Journal of Computational Physics 365 (2018) 294–323

Contents lists available at ScienceDirect

Journal of Computational Physics

www.elsevier.com/locate/jcp

A method of boundary equations for unsteady hyperbolic problems in 3D ☆

S. Petropavlovsky [a,b], S. Tsynkov [b,*], E. Turkel [c]

[a] National Research University Higher School of Economics, Moscow 101000, Russia
[b] Department of Mathematics, North Carolina State University, Box 8205, Raleigh, NC 27695, USA
[c] School of Mathematical Sciences, Tel Aviv University, Ramat Aviv, Tel Aviv 69978, Israel

ARTICLE INFO

Article history:
Received 2 January 2018
Received in revised form 23 March 2018
Accepted 26 March 2018
Available online 29 March 2018

Keywords:
Time-dependent wave equation
Calderon's boundary equation
The Huygens' principle
Method of difference potentials (MDP)
Sub-linear complexity
Parallelization in time

ABSTRACT

We consider interior and exterior initial boundary value problems for the three-dimensional wave (d'Alembert) equation. First, we reduce a given problem to an equivalent operator equation with respect to unknown sources defined only at the boundary of the original domain. In doing so, the Huygens' principle enables us to obtain the operator equation in a form that involves only finite and non-increasing pre-history of the solution in time. Next, we discretize the resulting boundary equation and solve it efficiently by the method of difference potentials (MDP). The overall numerical algorithm handles boundaries of general shape using regular structured grids with no deterioration of accuracy. For long simulation times it offers sub-linear complexity with respect to the grid dimension, i.e., is asymptotically cheaper than the cost of a typical explicit scheme. In addition, our algorithm allows one to share the computational cost between multiple similar problems. On multi-processor (multi-core) platforms, it benefits from what can be considered an effective parallelization in time.

1. Introduction

Numerical methods that rely on the boundary integral equations (BIEs) and are usually called boundary element methods (BEM) are popular for elliptic PDEs (steady-state or time-harmonic problems). Their key advantage is that they reduce the dimension of the problem by one (e.g., if the original formulation is three-dimensional, then the corresponding boundary integrals will be two-dimensional). Moreover, they offer a substantial flexibility from the standpoint of geometry so that the shape of the boundary can be quite general. In spite of their inherent limitations, such as the need to explicitly know the fundamental solution, the methods based on BIEs present a viable alternative to well-known volumetric methods, such as finite differences (FD) or finite elements (FEM). This is especially true for exterior problems where the variation of material properties is less of an issue and hence one can often use constant coefficient governing equations for which the fundamental solution is readily available. In that case, an additional advantage of BEM is that it automatically guarantees the correct behavior of the solution in the far field and therefore requires no artificial boundary conditions (ABCs).

☆ Work supported by the US Army Research Office (ARO) under grant # W911NF-16-1-0115, and by the US–Israel Binational Science Foundation (BSF) under grant # 2014048.

* Corresponding author at: Department of Mathematics, North Carolina State University, Box 8205, Raleigh, NC 27695, USA.
E-mail addresses: spetrop@ncsu.edu (S. Petropavlovsky), tsynkov@math.ncsu.edu (S. Tsynkov), turkel@post.tau.ac.il (E. Turkel).
URLs: http://www4.ncsu.edu/~stsynkov/ (S. Tsynkov), http://www.math.tau.ac.il/~turkel/ (E. Turkel).

https://doi.org/10.1016/j.jcp.2018.03.039
0021-9991/

The treatment of the actual physical boundary conditions in BEM requires case-by-case care. Indeed, the unknowns for BIEs, i.e., the boundary sources, should be chosen so as to maintain the equivalence of the original boundary value problem (BVP) to the BIE and well-posedness of the latter.[1] In particular, resonances of the complementary domain require special consideration [1].

Even though the well-posedness presents a delicate issue when setting the boundary conditions in BEM for elliptic PDEs (in those cases that go beyond the simplest scenarios), it has received substantial attention in the literature. In applications such as computational electromagnetism (CEM), the possible ill-posedness of the boundary representation may be alleviated, e.g., by the so-called combined field integral equations. A universal reduction from the domain to the boundary can be obtained with the help of Calderon's boundary projection operators [2,3]. It is not tied to any particular type of boundary conditions, as opposed to BIEs with respect to specific densities, such as that of a single-layer potential or double-layer potential. Importantly, it automatically preserves the well-posedness at the boundary as long as the original BVP is well-posed [4].

Unfortunately, the standard BEM cannot be applied directly to hyperbolic PDEs. Its time-dependent applications are rather limited to combined problems with a clearly identifiable elliptic component, such as low speed flows of viscous fluid [5,6] or water waves [7].

A special class of BIEs called the retarded potential boundary integral equations (RPBIEs) are designed at extending the BEM from elliptic to hyperbolic PDEs [8,9]. However, the corresponding time domain numerical methods, see, e.g., [10–13], have not gained nearly as much traction as their frequency domain (or pure potential) counterparts. One difficulty is that the time domain discretizations of RPBIEs often develop instabilities even if the RPBIE itself is well-posed (some aspects of stability have recently been studied in [14]). For the most part, however, the reason is that as the time elapses the boundary extends and the computation of convolutions involved in RPBIEs becomes progressively more expensive (it typically relies on Laplace transform methods [15,16]). An up-to-date comprehensive review of the entire area can be found in the recent monograph [13].

In the current work, we focus on presenting a new methodology that removes the foregoing main limitation of all numerical methods based on RPBIEs and convolution quadratures [17]. Namely, for a given interior or exterior hyperbolic initial boundary value problem (IBVP) we show how to equivalently reduce it from the domain to the boundary while explicitly taking into account the (strong) Huygens' principle. The Huygens' principle provides a mathematical characterization of the phenomenon of diffusionless propagation of waves. In the case of diffusionless propagation, the waves due to compactly supported sources (in space–time) have sharp aft (or trailing) fronts. The regions behind those aft fronts are known as secondary lacunae in the sense of Petrowsky [18–20]. The solution inside the secondary lacunae is identically equal to zero.

For the Huygens' principle to hold, the number of space dimensions must be odd. Moreover, there are additional rather tight constraints that altogether make the diffusionless propagation of waves a rare occurrence. It, however, manifests itself for the acoustic and electromagnetic waves in three space dimensions.[2] Remarkably, it is those two types of waves that appear in a broad range of applications in science and engineering. Moreover, in many instances both acoustic and electromagnetic waves allow for a simplified representation by means of the scalar wave (d'Alembert) equation. It is known that a scalar PDE in the conventional $3+1$-dimensional Minkowski space–time satisfies the Huygens' principle if and only if it reduces to the d'Alembert equation [22].

For both interior and exterior IBVPs for the three-dimensional wave equation, a key role played by the Huygens' principle is that it allows one to derive an equivalent boundary operator equation of Calderon's type with only a finite and non-increasing backward dependence on time. The advantage of Calderon's boundary equations with projections is that they operate with physical sources (traces of the solution and its normal derivative at the boundary) and are completely independent of the boundary conditions. It means that the same reduced boundary formulation can handle a wide variety of boundary conditions. Of central importance is that unlike in the typical RPBIEs [13] where the unknowns (boundary densities) are defined everywhere between the initial and current moment of time, the unknowns for Calderon's equations that we employ (i.e., Calderon's equation that rely on the Huygens' principle) are specified only on an interval of a fixed finite duration, regardless of the actual time that has elapsed since the initial moment. This property renders unnecessary the evaluation of convolutions over ever expanding time intervals.[3]

The limited backward dependence in time is important because the "finite-time" boundary operator equations can be solved efficiently. In our implementation, we use the method of difference potentials (MDP) [4] as a vehicle for discretization and numerical solution of the corresponding Calderon's boundary equations. The MDP is very well suited for this purpose as it parallels the constructs of Calderon's potentials and boundary projection operators at the discrete level. As in the continuous case, it guarantees that the resulting boundary formulation will be well-posed.

[1] In the classical potential theory, the reduction of a BVP from its domain to the boundary is contingent upon specific boundary conditions. For example, a Dirichlet problem requires boundary representation in the form of a double-layer potential, whereas a Neumann problem needs a single-layer potential. This guarantees that the corresponding BIE will be a Fredholm integral equation of the second kind, which is well-posed.

[2] In acoustics (linearized Euler's equations), diffusionless propagation characterizes the pressure waves as opposed to vorticity waves. In electromagnetism (Maxwell's equations), classical lacunae are sometimes replaced with quasi-lacunae inside which the solution is electrostatic yet not necessarily zero [21].

[3] According to [13, page 86], the convolution quadratures built via the Laplace transform "eliminate the Huygens' principle that so clearly appears in the time domain retarded operators and potentials."

The discrete counterparts of Calderon's potentials and Calderon's boundary projections are computed in the framework of MDP by means of solving a specially formulated auxiliary problem (AP). It replaces the convolution integrals that appear in the conventional definition of Calderon's operators. The AP is set up and solved on a volumetric grid. However, this grid can be chosen regular (e.g., Cartesian) for computational convenience, whereas the boundary can have a general non-conforming shape. Therefore, the MDP maintains the geometric flexibility typical for BEM. At the same time, it allows one to avoid the numerical computation of singular integrals. Moreover, MDP enables reducing the computational cost when solving multiple similar problems (e.g., problems that share the same geometry yet have different boundary conditions). If the MDP is combined with the Huygens' principle, the computational complexity of the resulting algorithm appears lower than that of the common explicit schemes. Moreover, in the case of a multi-processor (or multi-core) implementation, our algorithm essentially renders parallelization in time. We note that, while the MDP is our method of choice, the Calderon-type boundary equations that we built can be discretized and solved using other techniques as well.

The methodology we are proposing is not the first ever application of the Huygens' principle in scientific computing. Previously, lacunae and the Huygens' principle were used to design highly accurate ABCs for the numerical simulation of waves.[4] The pioneering work by Ryaben'kii dates back to 1990 [26]. Later, it has been generalized to the wave equation driven by moving sources [27], acoustics equations [28], and Maxwell's equations [29–31]. The main focus of the current work is to extend the application of lacunae beyond the artificial outer boundaries and include the various IBVPs with a broad range of boundary conditions set at the boundaries of general shape.

There is an alternative approach to solving unsteady problems by MDP. It was first explored in [32,33] for parabolic equations and then extended to the wave equation in our recent work [34]. The governing PDE is discretized by means of an implicit scheme (e.g., the compact high order accurate scheme [35]), which yields an elliptic (i.e., steady-state) equation at the upper time level. This equation is solved at each time step by the conventional MDP in much the same way as, e.g., the Helmholtz equation [36,37]. The resulting algorithm is simple and inexpensive. Moreover, as it does not rely on the Huygens' principle, it can be built in 2D and can handle variable coefficients (e.g., the propagation speed that varies in space) as easily as constant coefficients. This is an important advantage. There are, however, some limitations as well. The elliptic equation solved at each time step is inhomogeneous. Its source term comes from the previous time levels. Therefore, for an exterior problem this equation will remain inhomogeneous over the entire unbounded region. This is an obstacle for numerical solution. Furthermore, with no use of lacunae in the case of hyperbolic PDEs, this technique cannot offer sub-linear computational complexity.

The rest of the paper is organized as follows. Interior problems are analyzed in Section 2. Exterior problems are discussed in Section 3. A succinct account of the method of difference potentials as it applies to solving the corresponding unsteady boundary equations is given in Section 4. The results of numerical simulations are provided in Section 5. Section 6 summarizes the current findings and identifies the directions for future work. Appendix A presents the results of additional numerical simulations for the Neumann problem.

2. Interior problem

Let $\Box_c$ denote the d'Alembert operator with a constant propagation speed c:

$$\Box_c u \equiv \frac{1}{c^2}\frac{\partial^2 u}{\partial t^2} - \Delta u. \tag{1}$$

Consider the following initial boundary value problem:

$$\Box_c u(\boldsymbol{x}, t) = 0, \quad (\boldsymbol{x}, t) \in \Omega \times (0, T], \tag{2a}$$

$$u\big|_{t=0} = u_0(\boldsymbol{x}), \quad \frac{\partial u}{\partial t}\Big|_{t=0} = u_1(\boldsymbol{x}), \quad \boldsymbol{x} \in \Omega, \tag{2b}$$

$$\boldsymbol{l}_\Gamma u = \phi, \quad (\boldsymbol{x}, t) \in \Gamma \equiv \partial\Omega \times (0, T], \tag{2c}$$

where $\Omega \subset \mathbb{R}^3$ is a bounded domain with piece-wise smooth boundary $\partial\Omega$, T is the final time, and $\boldsymbol{l}_\Gamma$ is the operator of the boundary conditions. The wave equation (2a) is homogeneous. The boundary condition (2c) can be time-dependent. The entire IBVP (2) is assumed well-posed in the sense of the standard energy integrals, i.e., in the sense of L_2, see, e.g., [38,39]. This is the most common interpretation of well-posedness for linear hyperbolic IBVPs. The geometry of problem (2) is schematically shown in Fig. 1. Note that, while the actual formulation is three-dimensional, we are using the simplified 2D and 1D illustrations, see Figs. 1a and 1b, respectively.

2.1. Reduction to the boundary

The fundamental solution G of the 3D d'Alembert operator (1) satisfies equation $\Box_c G = \delta$. It is a single layer on the sphere of radius ct centered at the origin:

[4] Convolution quadratures have also been used for the development and analysis of far-field boundary conditions, see, e.g., [23], as well as the more recent work [24,25] that involves RPBIEs.

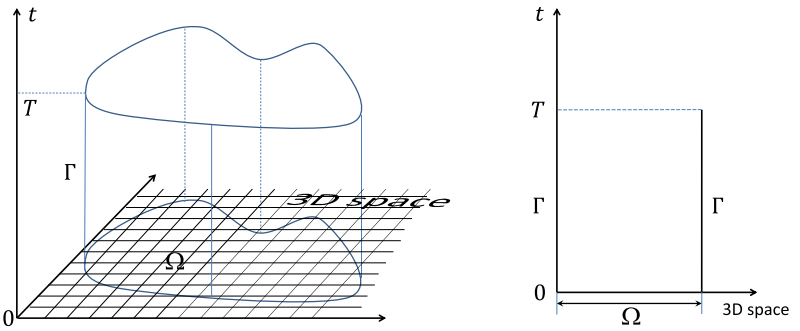

(a) 2D schematic: curvilinear cylinder $\Omega \times [0, T]$ (b) 1D schematic

Fig. 1. Geometry of the IBVP (2).

$$G(\boldsymbol{x}, t) = \frac{c}{2\pi}\theta(t)\delta(c^2t^2 - |\boldsymbol{x}|^2). \tag{3}$$

The Heaviside step function $\theta(t) \equiv \begin{cases} 0, & t \leqslant 0, \\ 1, & t > 0, \end{cases}$ on the right-hand side of (3) is a manifestation of causality — a source at $t = 0$ may affect the solution only at subsequent times, $t > 0$.

Let $u(\boldsymbol{x}, t)$ be any solution to the wave equation (2a), and let $\tilde{u}(\boldsymbol{x}, t)$ be its formal extension with zero beyond the cylinder $\Omega \times (0, T)$. Then, $\tilde{u} = G * \Box_c \tilde{u}$, which, in particular, implies that for any $(\boldsymbol{x}, t) \in \Omega \times (0, T)$ we can write the following Green's formula:

$$\begin{aligned} u(\boldsymbol{x}, t) = {} & \frac{1}{c^2}\int\limits_{\Omega} \left\{ \frac{\partial u}{\partial t}(\boldsymbol{y}, 0)G(\boldsymbol{x} - \boldsymbol{y}, t) - u(\boldsymbol{y}, 0)\frac{\partial G}{\partial t}(\boldsymbol{x} - \boldsymbol{y}, t) \right\} d\boldsymbol{y} \\ & - \frac{1}{c^2}\int\limits_{\Omega} \left\{ \frac{\partial u}{\partial t}(\boldsymbol{y}, T)G(\boldsymbol{x} - \boldsymbol{y}, t - T) - u(\boldsymbol{y}, T)\frac{\partial G}{\partial t}(\boldsymbol{x} - \boldsymbol{y}, t - T) \right\} d\boldsymbol{y} \\ & + \int\limits_{\Gamma} \left\{ \frac{\partial u}{\partial \boldsymbol{n}}(\boldsymbol{y}, t')G(\boldsymbol{x} - \boldsymbol{y}, t - t') - u(\boldsymbol{y}, t')\frac{\partial G}{\partial \boldsymbol{n}}(\boldsymbol{x} - \boldsymbol{y}, t - t') \right\} dt' dS_{\boldsymbol{y}}, \end{aligned} \tag{4}$$

where $\boldsymbol{n}$ is the outward normal to $\partial\Omega$ and $dS_{\boldsymbol{y}}$ corresponds to the integration over $\partial\Omega$. While we use the conventional integral notation in (4), the integrals need to be interpreted as convolutions in the sense of distributions, in accordance with the definition of G given by (3).

The second integral on the right-hand side of (4) vanishes because of the causality of G, see (3), since for $t \in (0, T)$ we have $t - T < 0$. Due to the same reason, the third integral can be calculated over only $\Gamma_t \equiv \partial\Omega \times (0, t]$ rather then over the entire Γ, where t is the current moment of time. This yields (cf. [40, equation (7.3.5)]):

$$\begin{aligned} u(\boldsymbol{x}, t) = {} & \frac{1}{c^2}\int\limits_{\Omega} \left\{ \frac{\partial u}{\partial t}(\boldsymbol{y}, 0)G(\boldsymbol{x} - \boldsymbol{y}, t) - u(\boldsymbol{y}, 0)\frac{\partial G}{\partial t}(\boldsymbol{x} - \boldsymbol{y}, t) \right\} d\boldsymbol{y} \\ & + \int\limits_{\Gamma_t} \left\{ \frac{\partial u}{\partial \boldsymbol{n}}(\boldsymbol{y}, t')G(\boldsymbol{x} - \boldsymbol{y}, t - t') - u(\boldsymbol{y}, t')\frac{\partial G}{\partial \boldsymbol{n}}(\boldsymbol{x} - \boldsymbol{y}, t - t') \right\} dt' dS_{\boldsymbol{y}}. \end{aligned} \tag{5}$$

Equation (5) is the well-known Green's formula for the wave equation (2a). It shows that in general the solution at a given $(\boldsymbol{x}, t) \in \Omega \times (0, T)$ is affected by both the initial data at $t = 0$ and the boundary data at Γ_t. Moreover, it indicates that having a pre-defined terminal time T is not essential, as the solution can be obtained by surface integrals for any given $t > 0$. For $\boldsymbol{x} \notin \bar{\Omega}$, formula (5) yields $u = 0$. Other Green's functions, besides the fundamental solution (3), can be used in (5), see [40, Section 7.3]. It may be beneficial for some purposes, including computational. Our current analysis, however, becomes most transparent when using the genuine free space Green's function (3). As the cylinder $(\boldsymbol{x}, t) \in \Omega \times (0, T)$ is a four-dimensional shape, all surface integrals in (5) are three-dimensional. By substituting the actual form of (3) and performing the integration dt' in the second integral of (5), one can reduce the latter to the retarded potential representation [13]. Yet for our purposes it will be more convenient to keep the Green's formula as given by (5).

Denote by B the bottom of the cylinder shown in Fig. 1a, i.e., the domain Ω at $t = 0$. Let $\boldsymbol{\xi}_{\mathrm{B}} = \left(u, \frac{\partial u}{\partial t}\right)\Big|_{\mathrm{B}} \equiv (u_0, u_1)$ be a vector function on B with two components given by the initial values of the solution and its first time derivative, see (2b). At the lateral boundary Γ_t, introduce another two-dimensional vector function, $\boldsymbol{\xi}_{\Gamma_t} = (\xi_0, \xi_1)$. Denote by $\boldsymbol{\Xi}_t = (\boldsymbol{\xi}_{\mathrm{B}}, \boldsymbol{\xi}_{\Gamma_t})$ the juxtaposition of these two vector functions. By analogy with the Green's formula (5), define a mapping $\mathcal{P}_\Omega$ that maps $\boldsymbol{\Xi}_t$ onto a "plain" scalar function of the arguments $(\boldsymbol{x}, t)$ on Ω:

$$\mathcal{P}_\Omega \Xi_t(\boldsymbol{x},t) = \underbrace{\frac{1}{c^2}\int\limits_\Omega \left\{u_1(\boldsymbol{y})G(\boldsymbol{x}-\boldsymbol{y},t) - u_0(\boldsymbol{y})\frac{\partial G}{\partial t}(\boldsymbol{x}-\boldsymbol{y},t)\right\} d\boldsymbol{y}}_{\boldsymbol{P}'_\Omega \boldsymbol{\xi}_{\mathrm{B}}(\boldsymbol{x},t)} + \underbrace{\int\limits_{\Gamma_t} \left\{\xi_1(\boldsymbol{y},t')G(\boldsymbol{x}-\boldsymbol{y},t-t') - \xi_0(\boldsymbol{y},t')\frac{\partial G}{\partial \boldsymbol{n}}(\boldsymbol{x}-\boldsymbol{y},t-t')\right\} dt' dS_{\boldsymbol{y}}}_{\boldsymbol{P}_\Omega \boldsymbol{\xi}_{\Gamma_t}(\boldsymbol{x},t)}. \tag{6}$$

Since, $\boldsymbol{\xi}_{\mathrm{B}} = (u_0, u_1)$ is assumed given and fixed while $\boldsymbol{\xi}_{\Gamma_t}$ can be arbitrary, the mapping $\mathcal{P}_\Omega$ introduced by (6) appears an affine mapping from the space of vector functions $\boldsymbol{\xi}_{\Gamma_t} = (\xi_0, \xi_1)$ defined on the boundary Γ_t to the space of ordinary functions of the arguments $(\boldsymbol{x}, t)$ on the domain Ω, $t > 0$.

The purely linear part of the mapping $\mathcal{P}_\Omega$ with respect to $\boldsymbol{\xi}_{\Gamma_t}$, which is given by the second integral on the right-hand side of (6) and denoted by $\boldsymbol{P}_\Omega \boldsymbol{\xi}_{\Gamma_t}(\boldsymbol{x}, t)$, is called Calderon's potential with the density $\boldsymbol{\xi}_{\Gamma_t}$. In the particular case where $\xi_0 = u\big|_{\Gamma_t}$ and $\xi_1 = \frac{\partial u}{\partial \boldsymbol{n}}\Big|_{\Gamma_t}$, the right-hand side of (6) coincides with that of (5) and accordingly, $\mathcal{P}_\Omega \Xi_t(\boldsymbol{x}, t)$ coincides with the solution $u(\boldsymbol{x}, t)$.

For future convenience, we recast equation (6) in the compact form:

$$\mathcal{P}_\Omega \Xi_t(\boldsymbol{x},t) = \boldsymbol{P}_\Omega \boldsymbol{\xi}_{\Gamma_t}(\boldsymbol{x},t) + \boldsymbol{P}'_\Omega \boldsymbol{\xi}_{\mathrm{B}}(\boldsymbol{x},t). \tag{6′}$$

The initial data $\boldsymbol{\xi}_{\mathrm{B}}$ in (6′) can be viewed as a known part of the overall density Ξ_t defined at the combined boundary $\Gamma_t \cup \mathrm{B}$. In that regard, the derivative $\frac{\partial}{\partial t}$ can be interpreted as the normal derivative at B. Unlike in the case of elliptic problems, where the density of a Calderon potential is defined over the entire boundary, see [4], the density in (6′) is defined only on a part. Namely, the boundary (cylinder) does not have the top portion, i.e., no density is defined at the current moment of time t. This is due to the causal nature of the Green's function (3). The solution to the IBVP (2) at t should be sought rather than specified ahead of time.

For any $\boldsymbol{\xi}_{\Gamma_t} = (\xi_0, \xi_1)$, the left-hand side of (6′) solves the homogeneous wave equation for $\boldsymbol{x} \in \Omega$ and $t > 0$:

$$\Box_c \mathcal{P}_\Omega \Xi_t = 0.$$

It also satisfies the initial conditions (2b). Likewise, for any $\boldsymbol{\xi}_{\Gamma_t} = (\xi_0, \xi_1)$ the Calderon potential given by the first term on the right-hand side of (6′) solves the wave equation (2a):

$$\Box_c \boldsymbol{P}_\Omega \boldsymbol{\xi}_{\Gamma_t} = 0$$

and satisfies the homogeneous initial conditions at $t = 0$.

However, in general neither $\boldsymbol{P}_\Omega \boldsymbol{\xi}_{\Gamma_t}$ nor $\mathcal{P}_\Omega \Xi_t$ coincide with the density $\boldsymbol{\xi}_{\Gamma_t}$. Introduce the vector trace operator on Γ_t:

$$\forall\, w(\boldsymbol{x},t): \quad \boldsymbol{Tr}_{\Gamma_t} w \stackrel{\mathrm{def}}{=} \left(w, \frac{\partial w}{\partial \boldsymbol{n}}\right)\Big|_{\Gamma_t}. \tag{7}$$

Then, unless $\boldsymbol{\xi}_{\Gamma_t}$ is the trace of a solution to equation (2a), we have:

$$\boldsymbol{Tr}_{\Gamma_t} \boldsymbol{P}_\Omega \boldsymbol{\xi}_{\Gamma_t} \neq \boldsymbol{\xi}_{\Gamma_t} \quad \text{and} \quad \boldsymbol{Tr}_{\Gamma_t} \mathcal{P}_\Omega \Xi_t \neq \boldsymbol{\xi}_{\Gamma_t}. \tag{8}$$

Relations (8) are a manifestation of the well-known fact that the boundary conditions for the wave equation cannot be set arbitrarily and simultaneously for both the solution itself and its normal derivative. Specifying u and $\frac{\partial u}{\partial \boldsymbol{n}}$ at the boundary would yield an overdetermined IBVP.

The left-hand side of the first relation (8) defines a very important operator — Calderon's projection:

$$\boldsymbol{P}_{\Gamma_t} \boldsymbol{\xi}_{\Gamma_t} \stackrel{\mathrm{def}}{=} \boldsymbol{Tr}_{\Gamma_t} \boldsymbol{P}_\Omega \boldsymbol{\xi}_{\Gamma_t}. \tag{9}$$

An argument similar to that given in [4] allows one to show that the following boundary equation with projection (BEP)

$$\boldsymbol{P}_{\Gamma_t} \boldsymbol{\xi}_{\Gamma_t} = \boldsymbol{\xi}_{\Gamma_t} \tag{10}$$

holds if and only if $\boldsymbol{\xi}_{\Gamma_t} = \boldsymbol{Tr}_{\Gamma_t} u$, where $u(\boldsymbol{x}, t)$ is a solution to the wave equation (2a) subject to zero initial conditions at $t = 0$. Moreover, the inhomogeneous BEP

$$\boldsymbol{P}_{\Gamma_t} \boldsymbol{\xi}_{\Gamma_t} + \boldsymbol{Tr}_{\Gamma_t} \boldsymbol{P}'_\Omega \boldsymbol{\xi}_{\mathrm{B}} = \boldsymbol{\xi}_{\Gamma_t} \tag{10′}$$

with $\boldsymbol{\xi}_{\mathrm{B}} = (u_0, u_1)$ holds if and only if $\boldsymbol{\xi}_{\Gamma_t} = \boldsymbol{Tr}_{\Gamma_t} u$, where $u(\boldsymbol{x}, t)$ is a solution to the wave equation (2a) subject to the initial conditions (2b).

The BEP (10′) with the operator $\boldsymbol{P}_{\Gamma_t}$ defined by (9) can be considered an equation for the unknown density $\boldsymbol{\xi}_{\Gamma_t}$, where the term $\boldsymbol{Tr}_{\Gamma_t}\boldsymbol{P}'_{\Omega}\boldsymbol{\xi}_{\mathrm{B}}$ is a known source term that accounts for the inhomogeneous initial conditions (2b). To find the specific $\boldsymbol{\xi}_{\Gamma_t}$ that corresponds to the original IBVP (2), one also needs to take into account the boundary condition (2c). For convenience, we recast it as

$$\boldsymbol{l}_{\Gamma_t}\boldsymbol{\xi}_{\Gamma_t} = \phi, \tag{11}$$

emphasizing that the boundary condition is formulated on the interval from the initial to the current moment of time, and the operator $\boldsymbol{l}_{\Gamma_t}$ acts on vector densities $\boldsymbol{\xi}_{\Gamma_t}$ with the components ξ_0 and ξ_1 that correspond to the trace of the solution and its first normal derivative, respectively.

The simplest cases are those with Dirichlet and Neumann boundary conditions. In the Dirichlet case, the component ξ_0 in (11) is known, while ξ_1 needs to be determined in the course of the solution. The Neumann case is opposite, ξ_1 is known whereas ξ_0 should be determined. If (11) is a mixed (Robin) boundary condition, then it implies a relation between ξ_0 and ξ_1 on Γ_t. In general, regardless of the specific type of the boundary condition, equation (11) is combined with the BEP (10′). The resulting system (10′), (11) is equivalent to the IBVP (2) yet formulated only at the boundary. It is to be solved with respect to the unknown boundary density $\boldsymbol{\xi}_{\Gamma_t}$. Once the density $\boldsymbol{\xi}_{\Gamma_t}$ has been determined, it is substituted on the right-hand side of equation (6′) (along with the initial data $\boldsymbol{\xi}_{\mathrm{B}}$), which yields the solution u to IBVP (2) on the domain Ω at the time t.

A key advantage of using Calderon's operators is that they render the reduction of the wave equation/initial conditions (2a)–(2b) to the boundary in the form of the BEP (10′) completely independent of the boundary condition (11). The latter is "added" to the resulting BEP to form the overall boundary system that is solved with respect to $\boldsymbol{\xi}_{\Gamma_t}$. Hence, Calderon's operators provide a very substantial flexibility from the standpoint of handling a variety of boundary conditions.

The rationale for using the boundary reformulation (10′)–(11), as opposed to solving IBVP (2) directly, is the reduced dimensionality.[5] Indeed, both integrals on the right-hand side of (6) are three-dimensional, while the domain $\Omega \times (0, T)$ of the original problem (2) is four-dimensional. However, unlike in the conventional BEM for elliptic problems, the lateral boundary Γ_t, on which the unknowns $\boldsymbol{\xi}_{\Gamma_t}$ are specified, extends as the time t elapses. Therefore, the solution of system (10′), (11) with respect to $\boldsymbol{\xi}_{\Gamma_t}$ will be progressively more expensive for longer simulation times. This is a serious difficulty for practical implementation. It is a difficulty of the same type as encountered by numerical methods based on RPBIEs and convolution quadratures [13]. In Sections 2.2 and 2.3, we show how one can use the partition in time and Huygens' principle to completely remove this difficulty.

2.2. Partition in time

Let T_0 be a fixed time interval (to be specified later, see Section 2.3), and assume, with no loss of generality, that we are interested in obtaining the solution for $0 \leqslant t \leqslant K \cdot T_0 \equiv T$, where K is an integer.[6] Then, we partition the lateral boundary $\Gamma \equiv \Gamma_T$ into K equal parts:

$$\Gamma_T = \Gamma_1 \cup \Gamma_2 \cup \ldots \cup \Gamma_K, \tag{12a}$$

where

$$\Gamma_1 = \partial\Omega \times (0, T_0], \quad \Gamma_2 = \partial\Omega \times (T_0, 2T_0], \quad \ldots \quad \Gamma_K = \partial\Omega \times ((K-1)T_0, KT_0]. \tag{12b}$$

The density is partitioned accordingly:

$$\boldsymbol{\xi}_{\Gamma_T} = \boldsymbol{\xi}_{\Gamma_1} + \boldsymbol{\xi}_{\Gamma_2} + \ldots + \boldsymbol{\xi}_{\Gamma_K}, \tag{13}$$

where for $k = 1, 2, \ldots, K$:

$$\boldsymbol{\xi}_{\Gamma_k}(\boldsymbol{x}, t) = \begin{cases} \boldsymbol{\xi}_{\Gamma_T}(\boldsymbol{x}, t), & \text{if } (\boldsymbol{x}, t) \in \Gamma_k, \\ \boldsymbol{0}, & \text{if } (\boldsymbol{x}, t) \in \Gamma_T \backslash \Gamma_k. \end{cases} \tag{14}$$

In other words, whereas the boundary itself is split into non-overlapping segments according to (12), the density is represented as the linear combination (13), where each $\boldsymbol{\xi}_{\Gamma_k}$ is defined on the entire Γ_T yet may be non-zero only on the respective Γ_k: $\boldsymbol{\xi}_{\Gamma_k} \neq \boldsymbol{0}$, $k = 1, 2, \ldots K$, see Fig. 2a.

Equations (10′) and (11) written for the unknown density $\boldsymbol{\xi}_{\Gamma_T}$ take the form:

$$\boldsymbol{P}_{\Gamma_T}\boldsymbol{\xi}_{\Gamma_T} + \boldsymbol{Tr}_{\Gamma_T}\boldsymbol{P}'_{\Omega}\boldsymbol{\xi}_{\mathrm{B}} = \boldsymbol{\xi}_{\Gamma_T} \tag{15}$$

and

[5] This is true in regard to any method based on boundary equations, including RPBIEs [13].

[6] Having a pre-determined final time T is not essential, and larger T's can be accommodated by increasing K.

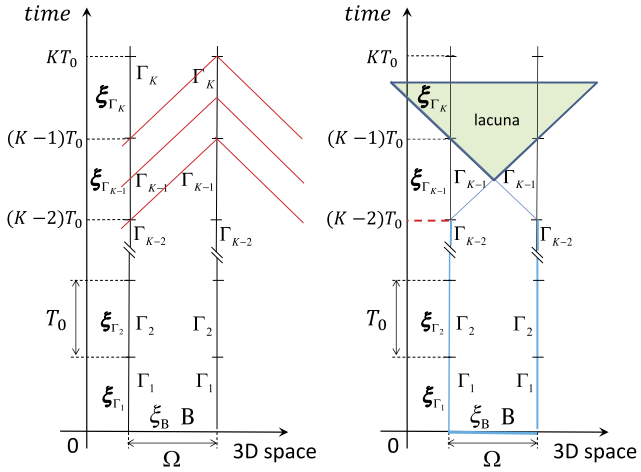

(a) Partition in time (b) Lacuna in the solution

Fig. 2. Partition in time and application of the Huygens' principle. Left panel: The characteristic cones are shown in red. Right panel: The solution is driven by (singular) sources at the lateral boundary and the bottom of the cylinder (shown in cyan); the sources operate until $t = (K-2)T_0$. (For interpretation of the colors in the figure(s), the reader is referred to the web version of this article.)

$$\boldsymbol{l}_{\Gamma_T}\boldsymbol{\xi}_{\Gamma_T} = \phi, \tag{16}$$

respectively, where $\boldsymbol{\xi}_{\mathrm{B}} = (u_0, u_1)$ is the initial data from (2b). Our goal is to reformulate equations (15)–(16) to allow for a consecutive determination of the partial densities $\boldsymbol{\xi}_{\Gamma_k}$. Specifically, we will derive the equations for the unknown partial density $\boldsymbol{\xi}_{\Gamma_K}$ assuming that the densities $\boldsymbol{\xi}_{\Gamma_k}$ for $k = 1, 2, \ldots, K-1$ have been found previously.

Hence, we use the definitions of Calderon's potential (6), boundary trace (7), and Calderon's projection (9), and split equation (15) into two by separating the last component Γ_K in the composition (12a) from the rest of the boundary Γ_T:

$$\boldsymbol{Tr}_{\Gamma_{T-T_0}}\boldsymbol{P}_\Omega\boldsymbol{\xi}_{\Gamma_T} + \boldsymbol{Tr}_{\Gamma_{T-T_0}}\boldsymbol{P}'_\Omega\boldsymbol{\xi}_{\mathrm{B}} = \boldsymbol{\xi}_{\Gamma_{T-T_0}}, \tag{17a}$$

$$\boldsymbol{Tr}_{\Gamma_K}\boldsymbol{P}_\Omega\boldsymbol{\xi}_{\Gamma_T} + \boldsymbol{Tr}_{\Gamma_K}\boldsymbol{P}'_\Omega\boldsymbol{\xi}_{\mathrm{B}} = \boldsymbol{\xi}_{\Gamma_K}. \tag{17b}$$

In equation (17a), $\Gamma_{T-T_0} = \Gamma_1 \cup \Gamma_2 \cup \ldots \cup \Gamma_{K-1}$, $\boldsymbol{\xi}_{\Gamma_{T-T_0}} = \boldsymbol{\xi}_{\Gamma_t}\big|_{t=T-T_0}$, and the trace operator is defined as $\boldsymbol{Tr}_{\Gamma_{T-T_0}} = \boldsymbol{Tr}_{\Gamma_t}$ for $t = T - T_0$. Similarly, the operator $\boldsymbol{Tr}_{\Gamma_K}$ in equation (17b) is the same trace operator as in (7) but taken only at the partial boundary Γ_K. The argument of $\boldsymbol{P}_\Omega$ on the left-hand side of each equation (17) is still the entire density $\boldsymbol{\xi}_{\Gamma_T}$.

However, due to the causality, equation (17a) will not change if one substitutes $\boldsymbol{\xi}_{\Gamma_{T-T_0}}$ instead of $\boldsymbol{\xi}_{\Gamma_T}$ on its left-hand side. This yields:

$$\boldsymbol{P}_{\Gamma_{T-T_0}}\boldsymbol{\xi}_{\Gamma_{T-T_0}} + \boldsymbol{Tr}_{\Gamma_{T-T_0}}\boldsymbol{P}'_\Omega\boldsymbol{\xi}_{\mathrm{B}} = \boldsymbol{\xi}_{\Gamma_{T-T_0}}, \tag{18}$$

where the projection $\boldsymbol{P}_{\Gamma_{T-T_0}}$ is defined according to (9) for $t = T - T_0$, i.e., $\boldsymbol{P}_{\Gamma_{T-T_0}} = \boldsymbol{P}_{\Gamma_t}\big|_{t=T-T_0}$. Clearly, equation (18) is basically the same as (15), except that the domain Γ_{T-T_0} for (18) is "shorter" and the domain Γ_T for (15) is "taller," see Fig. 2a. Equation (18) can be supplemented by the corresponding "truncated" counterpart of the boundary condition (16):

$$\boldsymbol{l}_{\Gamma_{T-T_0}}\boldsymbol{\xi}_{\Gamma_{T-T_0}} = \phi. \tag{19}$$

The system of equations (18), (19) is a system that determines $\boldsymbol{\xi}_{\Gamma_{T-T_0}}$.

Assume that the density $\boldsymbol{\xi}_{\Gamma_{T-T_0}}$ has been obtained by solving equations (18), (19). This means, in particular, that the partial densities $\boldsymbol{\xi}_{\Gamma_k}$ can be considered known for $k = 1, 2, \ldots, K-1$. We will show how to use equation (17b) to find the remaining partial density $\boldsymbol{\xi}_{\Gamma_K}$. We will show how to find the next partial density if the previous ones are available, which essentially yields a marching algorithm with respect to the partition index K.

Given that all $\boldsymbol{\xi}_{\Gamma_k}$, $k = 1, 2, \ldots, K-1$, are assumed known, we use the linearity and transform equation (17b) as follows:

$$\boldsymbol{Tr}_{\Gamma_K}\boldsymbol{P}_\Omega\boldsymbol{\xi}_{\Gamma_K} + \sum_{k=1}^{K-1}\boldsymbol{Tr}_{\Gamma_K}\boldsymbol{P}_\Omega\boldsymbol{\xi}_{\Gamma_k} + \boldsymbol{Tr}_{\Gamma_K}\boldsymbol{P}'_\Omega\boldsymbol{\xi}_{\mathrm{B}} = \boldsymbol{\xi}_{\Gamma_K}. \tag{20}$$

The second term on the left-hand side of (20), which is a sum from $k = 1$ through $K-1$, can be regarded as known because it represents the previously determined partial densities $\boldsymbol{\xi}_{\Gamma_k}$. The third term is also known as it represents the initial data $\boldsymbol{\xi}_{\mathrm{B}}$. Hence, equation (20) becomes an equation with respect to the unknown partial density $\boldsymbol{\xi}_{\Gamma_K}$.

Recall that $\boldsymbol{\xi}_{\Gamma_K}$ is defined on the entire lateral boundary Γ_T. However, it may differ from zero only on Γ_K, see (12) and (14). Then, according to (6), for the potential $\boldsymbol{P}_\Omega \boldsymbol{\xi}_{\Gamma_K}$ in the first term on the left-hand side of (20) we have:

$$\boldsymbol{P}_\Omega \boldsymbol{\xi}_{\Gamma_K}(\boldsymbol{x},t) = \int\limits_{T-T_0}^{T} \left\{ \xi_1(\boldsymbol{y},t') G(\boldsymbol{x}-\boldsymbol{y}, t-t') - \xi_0(\boldsymbol{y},t') \frac{\partial G}{\partial \boldsymbol{n}}(\boldsymbol{x}-\boldsymbol{y}, t-t') \right\} dt' dS_{\boldsymbol{y}}.$$

The density $\boldsymbol{\xi}_{\Gamma_K}(\boldsymbol{x},t)$, $\boldsymbol{x} \in \partial\Omega$, $(K-1)T_0 < t \leqslant KT_0$, can be thought of as a translation in time:

$$\boldsymbol{\xi}_{\Gamma_K}(\boldsymbol{x},t) = \boldsymbol{\xi}_{\Gamma_{T_0}}(\boldsymbol{x}, t-(K-1)T_0), \tag{21}$$

where $\boldsymbol{\xi}_{\Gamma_{T_0}}(\boldsymbol{x},\tilde{t})$ is a density defined for $0 < \tilde{t} \leqslant T_0$ as in Section 2.1. The kernel $G(\,\cdot\,, t-t')$ also allows translation in time, i.e., it depends only on the difference of the arguments $t-t'$, see (3). Then, we can recast the expression for the potential as follows:

$$\begin{aligned} \boldsymbol{P}_\Omega \boldsymbol{\xi}_{\Gamma_K}(\boldsymbol{x}, \tilde{t} + T_0(K-1)) &= \boldsymbol{P}_\Omega \boldsymbol{\xi}_{\Gamma_{T_0}}(\boldsymbol{x},\tilde{t}) \\ &= \int\limits_0^{T_0} \left\{ \xi_1(\boldsymbol{y},\tilde{t}') G(\boldsymbol{x}-\boldsymbol{y}, \tilde{t}-\tilde{t}') - \xi_0(\boldsymbol{y},\tilde{t}') \frac{\partial G}{\partial \boldsymbol{n}}(\boldsymbol{x}-\boldsymbol{y}, \tilde{t}-\tilde{t}') \right\} d\tilde{t}' dS_{\boldsymbol{y}}, \end{aligned}$$

where $0 < \tilde{t} \leqslant T_0$. Consequently, equation (20) becomes:

$$\boldsymbol{P}_{\Gamma_{T_0}} \boldsymbol{\xi}_{\Gamma_K} + \sum_{k=1}^{K-1} \boldsymbol{Tr}_{\Gamma_K} \boldsymbol{P}_\Omega \boldsymbol{\xi}_{\Gamma_k} + \boldsymbol{Tr}_{\Gamma_K} \boldsymbol{P}'_\Omega \boldsymbol{\xi}_{\mathrm{B}} = \boldsymbol{\xi}_{\Gamma_K}, \tag{20′}$$

where the operator $\boldsymbol{P}_{\Gamma_{T_0}}$ does not depend on K:

$$\boldsymbol{P}_{\Gamma_{T_0}} = \boldsymbol{P}_{\Gamma_t}\Big|_{t=T_0},$$

and $\boldsymbol{P}_{\Gamma_t}$ is defined according to (9) and (7). Hereafter, we will use the foregoing interpretation of the partial density as a translation in time, see (21), whenever it does not cause any confusion.

Equation (20′) needs to be supplemented by the respective fragment of the boundary condition:

$$\boldsymbol{l}_{\Gamma_K} \boldsymbol{\xi}_{\Gamma_K} = \phi. \tag{22}$$

Since, in general the boundary condition (16) is allowed to be time-dependent, in equation (22) we use the operator $\boldsymbol{l}_{\Gamma_K}$ rather than $\boldsymbol{l}_{\Gamma_{T_0}}$. The system of equations (20′), (22) determines $\boldsymbol{\xi}_{\Gamma_K}$. This completes the solution for the entire time interval of length $T = KT_0$. As, however, we have mentioned previously, the final time T is arbitrary. Hence, once $\boldsymbol{\xi}_{\Gamma_K}$ has been determined, we can use the same methodology to obtain yet another partial density, $\boldsymbol{\xi}_{\Gamma_{K+1}}$. Algorithmically, this amounts to replacing K with $K+1$ in equations (20′), (22) and effectively yields a time-marching procedure with respect to K.

We emphasize though that according to equation (20′), its solution $\boldsymbol{\xi}_{\Gamma_K}$ depends on all the preceding densities $\boldsymbol{\xi}_{\Gamma_k}$, $k = 1, \ldots, K-1$, as well as the initial data $\boldsymbol{\xi}_{\mathrm{B}}$. This is not surprising, because the system (20′), (22) for $\boldsymbol{\xi}_{\Gamma_K}$, along with the system (18), (19) for $\boldsymbol{\xi}_{\Gamma_{T-T_0}}$, present an equivalent reformulation of the overall system (15), (16). So the solution at later moments of time depends on its entire temporal pre-history. This property holds for any linear evolution problem. However, for the wave equation that satisfies the Huygens' principle, the dependence of $\boldsymbol{\xi}_{\Gamma_K}$ on $\boldsymbol{\xi}_{\Gamma_k}$, $k = 1, \ldots, K-1$, can be truncated. In Section 2.3, we explain how that can be done with the help of lacunae in the solution.

2.3. Application of Huygens' principle

Let the size T_0 of the partition (12) be chosen as

$$T_0 \geqslant \frac{1}{c} \operatorname{diam} \Omega. \tag{23}$$

As the integrals on the right-hand side of (6) are convolutions with the free space Green's function (3), it is easy to see that for any $(\boldsymbol{x},t) \in \Gamma_K$, there will be no contribution from the initial data $\boldsymbol{\xi}_{\mathrm{B}}$ on the left-hand side of equation (20′) and no contribution from any $\boldsymbol{\xi}_{\Gamma_k}$ either for $k = 1, 2, \ldots, K-2$. The only source term remaining on the left-hand side of (20′) will be $\boldsymbol{Tr}_{\Gamma_K} \boldsymbol{P}_\Omega \boldsymbol{\xi}_{\Gamma_{K-1}}$. This happens because if the vertex of a characteristic cone belongs to Γ_K, then its surface does not intersect with the bottom B and does not intersect with any of the segments Γ_k either for $k = 1, 2, \ldots, K-2$, see Fig. 2a. The surface of such a cone may intersect only with Γ_{K-1}. For this phenomenon to hold, the space must be three-dimensional and the size of the partition must satisfy (23).

Then, equation (20′) transforms into

$$\boldsymbol{P}_{\Gamma_{T_0}}\boldsymbol{\xi}_{\Gamma_K} + \boldsymbol{T}\boldsymbol{r}_{\Gamma_K}\boldsymbol{P}_{\Omega}\boldsymbol{\xi}_{\Gamma_{K-1}} = \boldsymbol{\xi}_{\Gamma_K}, \tag{20″}$$

and we observe that $\boldsymbol{\xi}_{\Gamma_K}$ depends only on one immediately preceding partial density $\boldsymbol{\xi}_{\Gamma_{K-1}}$ rather than on all $\boldsymbol{\xi}_{\Gamma_k}$. The second term on the left-hand side of equation (20″) involves the evaluation of Calderon's projection due to a given partial density $\boldsymbol{\xi}_{\Gamma_{K-1}}$ and taking its boundary trace (7) at the subsequent partition element Γ_K. For future convenience, we denote the overall operator by $\boldsymbol{R}_{\Gamma_{T_0}}$:

$$\boldsymbol{R}_{\Gamma_{T_0}}\boldsymbol{\xi}_{\Gamma_{K-1}}(\boldsymbol{x},t) = \boldsymbol{T}\boldsymbol{r}_{\Gamma_K}\int\limits_{T-2T_0}^{T-T_0}\left\{\xi_1(\boldsymbol{y},t')G(\boldsymbol{x}-\boldsymbol{y},t-t') - \xi_0(\boldsymbol{y},t')\frac{\partial G}{\partial \boldsymbol{n}}(\boldsymbol{x}-\boldsymbol{y},t-t')\right\}dt'dS_{\boldsymbol{y}},$$
$$\boldsymbol{x}\in\partial\Omega, \quad T-T_0 < t \leqslant T. \tag{24}$$

Due to the same argument as given in Section 2.2 when deriving equation (20′), the operator $\boldsymbol{R}_{\Gamma_{T_0}}$ does not depend on K, i.e., admits translation in time. Therefore, equation (20″) becomes:

$$\boldsymbol{P}_{\Gamma_{T_0}}\boldsymbol{\xi}_{\Gamma_K} + \boldsymbol{R}_{\Gamma_{T_0}}\boldsymbol{\xi}_{\Gamma_{K-1}} = \boldsymbol{\xi}_{\Gamma_K}. \tag{25}$$

To calculate $\boldsymbol{\xi}_{\Gamma_K}$, equation (25) must be combined with (22). System (22), (25) allows one to update the partial density consecutively, i.e., by transitioning from $K-1$ to K. This procedure can be thought of as time stepping, with the size, i.e., duration, of each step equal to T_0. In doing so, to obtain the density $\boldsymbol{\xi}_{\Gamma_K}$ for the current step K, the required input consists of the density $\boldsymbol{\xi}_{\Gamma_{K-1}}$ from only one previous step, $K-1$, as well as the boundary data ϕ from the current step K. The foregoing time marching is performed along a $(2+1)$-dimensional lateral boundary, as opposed to the $(3+1)$-dimensional integration by a volumetric method. At some point, such as the final time $T = KT_0$, we may need to actually obtain the solution u on the entire domain Ω rather than only its trace at the boundary. This solution will be given by Calderon's potential:

$$u(\boldsymbol{x},T) = \boldsymbol{P}_{\Omega}\boldsymbol{\xi}_{\Gamma_K}. \tag{26}$$

The limited backward time dependence that allowed us to replace equation (20′) with equation (25) is a direct consequence of the presence of lacunae in the solutions of the wave equation. Indeed, for the sources located at the bottom B (initial conditions), as well as at the lateral boundary Γ below $t = T - 2T_0$ (i.e., at $\Gamma_{T-2T_0} = \Gamma_1 \cup \Gamma_2 \cup \ldots \cup \Gamma_{K-2}$), the domain Ω completely falls into the lacuna starting from $t = T - T_0$, see Fig. 2b. For a more detailed discussion of lacunae, their application to the construction of artificial boundary conditions, and generalization to Maxwell's equations, we refer the reader to our work [21,30,31].

We also emphasize that the actual solution to the IBVP (2) does not usually have lacunae as the waves generated by the initial and boundary conditions will keep bouncing off the boundaries and will thus remain inside Ω as the time elapses. However, the proposed boundary reformulation is based on Calderon's operators that are built with the help of the free space Green's function. Therefore, it allows us to take advantage of the Huygens' principle and thus obtain the foregoing two-step time-marching algorithm (25)–(22). In the next section, we introduce its semi-discrete version.

2.4. Semi-discretization

We consider two consecutive partition elements, say, $(K-1)$-th and K-th. The corresponding densities $\boldsymbol{\xi}_{\Gamma_K}$ and $\boldsymbol{\xi}_{\Gamma_{K-1}}$ can be expanded on Γ_K and Γ_{K-1} using an appropriate basis:

$$\boldsymbol{\xi}_{\Gamma_{K-1}} = \sum_s c^{(\mathrm{I})}_{0,s}\boldsymbol{\psi}_{0,s} + c^{(\mathrm{I})}_{1,s}\boldsymbol{\psi}_{1,s}, \quad \boldsymbol{\xi}_{\Gamma_K} = \sum_s c^{(\mathrm{II})}_{0,s}\boldsymbol{\psi}_{0,s} + c^{(\mathrm{II})}_{1,s}\boldsymbol{\psi}_{1,s}. \tag{27}$$

In formulae (27), the bi-component basis functions $\boldsymbol{\psi}_{0,s} = (\psi_s, 0)$ and $\boldsymbol{\psi}_{1,s} = (0, \psi_s)$ are used for representing the solution and its normal derivative, respectively. In practice, it is convenient and economical to choose the same basis functions on both Γ_{K-1} and Γ_K (recall, these boundary segments have the same duration T_0). This is what we assume in formulae (27), where the superscripts (I) and (II) indicate that the expansion coefficients pertain to Γ_{K-1} and Γ_K, respectively. As both Γ_{K-1} and Γ_K are Cartesian products of the spatial boundary $\partial\Omega$ times the corresponding time intervals, see formula (12b), it is also convenient to consider the basis functions $\boldsymbol{\psi}_{0,s}$ and $\boldsymbol{\psi}_{1,s}$ in (27) as products of functions that depend only on time and functions that depend only on space variables. The temporal factors are natural to take in the form of the Chebyshev polynomials. The spatial factors are determined by the geometry of $\partial\Omega$; for the simple spherical shape of $\partial\Omega$ analyzed in the current paper we use spherical harmonics, see Section 5.1. Moreover, for actual implementation the dimension of the basis is always chosen finite (see Sections 4.6 and 5.1). Then, expansions (27) can be understood, e.g., as Galerkin-type approximations that provide sufficient accuracy.

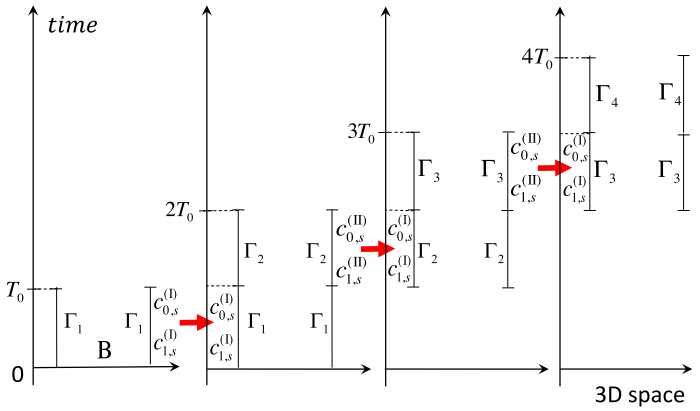

Fig. 3. Schematic for the time-marching algorithm based on equations (28)–(29).

Suppose the density $\boldsymbol{\xi}_{\Gamma_{K-1}}$ at the lower partition element is known, i.e., the coefficients $c^{(\mathrm{I})}_{0,s}$ and $c^{(\mathrm{I})}_{1,s}$ are available. Substituting expressions (27) into equation (25), we obtain:

$$\begin{aligned}\sum_s c^{(\mathrm{II})}_{0,s} \underbrace{\left\{\boldsymbol{P}_{\Gamma_{T_0}} - \boldsymbol{I}\right\}}_{\boldsymbol{Q}_{\Gamma_{T_0}}} \boldsymbol{\psi}_{0,s} + c^{(\mathrm{II})}_{1,s} \underbrace{\left\{\boldsymbol{P}_{\Gamma_{T_0}} - \boldsymbol{I}\right\}}_{\boldsymbol{Q}_{\Gamma_{T_0}}} \boldsymbol{\psi}_{1,s} \\ = -\sum_s c^{(\mathrm{I})}_{0,s} \boldsymbol{R}_{\Gamma_{T_0}} \boldsymbol{\psi}_{0,s} + c^{(\mathrm{I})}_{1,s} \boldsymbol{R}_{\Gamma_{T_0}} \boldsymbol{\psi}_{1,s},\end{aligned} \tag{28}$$

where $\boldsymbol{I}$ is the identity operator. In addition, the boundary condition (22) on Γ_K yields:

$$\boldsymbol{I}_{\Gamma_K} \sum_s c^{(\mathrm{II})}_{0,s} \boldsymbol{\psi}_{0,s} + c^{(\mathrm{II})}_{1,s} \boldsymbol{\psi}_{1,s} = \phi \equiv \sum_s c^{(\phi)}_s \psi_s. \tag{29}$$

If (22) is a Dirichlet boundary condition, then formula (29) implies that the coefficients $c^{(\mathrm{II})}_{0,s}$ are known and equal to the coefficients $c^{(\phi)}_s$ of the expansion of the Dirichlet data ϕ with respect to the same system of scalar basis functions ψ_s. Likewise, if (22) is a Neumann boundary condition, then the coefficients $c^{(\mathrm{II})}_{1,s}$ are equal to the known coefficients $c^{(\phi)}_s$ of the expansion of the Neumann data ϕ with respect to the basis functions ψ_s. For more general boundary conditions, e.g., Robin, formula (29) yields additional relations between the coefficients $c^{(\mathrm{II})}_{0,s}$ and $c^{(\mathrm{II})}_{1,s}$ that supplement equation (28).

In system (28), (29), the coefficients $c^{(\mathrm{II})}_{0,s}$ and $c^{(\mathrm{II})}_{1,s}$ are the unknowns, whereas $c^{(\mathrm{I})}_{0,s}$, $c^{(\mathrm{I})}_{1,s}$, and $c^{(\phi)}_s$ represent the data. Given the functions $\boldsymbol{Q}_{\Gamma_{T_0}} \boldsymbol{\psi}_{0,s}$ and $\boldsymbol{Q}_{\Gamma_{T_0}} \boldsymbol{\psi}_{1,s}$, solving this system means finding the coefficients of the linear combination on the first line of (28) that would make it equal to a known right-hand side (the second line of (28)), subject to additional constraints (29).

It is important that the operators $\boldsymbol{Q}_{\Gamma_{T_0}}$ and $\boldsymbol{R}_{\Gamma_{T_0}}$ do not depend on K, and the basis functions $\boldsymbol{\psi}_{0,s}$ and $\boldsymbol{\psi}_{1,s}$ are also chosen the same for all K. Consequently, the functions $\boldsymbol{Q}_{\Gamma_{T_0}} \boldsymbol{\psi}_{0,s}$, $\boldsymbol{Q}_{\Gamma_{T_0}} \boldsymbol{\psi}_{1,s}$, as well as $\boldsymbol{R}_{\Gamma_{T_0}} \boldsymbol{\psi}_{0,s}$, $\boldsymbol{R}_{\Gamma_{T_0}} \boldsymbol{\psi}_{1,s}$, remain unchanged for any two consecutive partition elements $K-1$ and K. This leads to the following time-marching algorithm with respect to K.

First, the system of equations (15), (16) is solved for $T = T_0$ or, equivalently, for $K = 1$. Then, we choose $K = 2$ and for $\boldsymbol{\xi}_{\Gamma_{K-1}} \equiv \boldsymbol{\xi}_{\Gamma_1}$ obtain the expansion coefficients $c^{(\mathrm{I})}_{0,s}$ and $c^{(\mathrm{I})}_{1,s}$ according to the first equality of (27). Next, we solve equations (28), (29) with respect to the coefficients $c^{(\mathrm{II})}_{0,s}$ and $c^{(\mathrm{II})}_{1,s}$ that are attributed to $\boldsymbol{\xi}_{\Gamma_K} \equiv \boldsymbol{\xi}_{\Gamma_2}$. After that, we perform one time step. Namely, the upper level coefficients become the lower level coefficients: $c^{(\mathrm{I})}_{0,s} \leftarrow\!\shortmid c^{(\mathrm{II})}_{0,s}$, $c^{(\mathrm{I})}_{1,s} \leftarrow\!\shortmid c^{(\mathrm{II})}_{1,s}$ and system (28), (29) is solved again, this time with respect to the expansion coefficients $c^{(\mathrm{II})}_{0,s}$ and $c^{(\mathrm{II})}_{1,s}$ for $\boldsymbol{\xi}_{\Gamma_K} \equiv \boldsymbol{\xi}_{\Gamma_3}$. The same process continues further, i.e., for $K = 4, 5, \ldots$, as schematically shown in Fig. 3. In doing so, neither the functions $\boldsymbol{Q}_{\Gamma_{T_0}} \boldsymbol{\psi}_{0,s}$, $\boldsymbol{Q}_{\Gamma_{T_0}} \boldsymbol{\psi}_{1,s}$ that form the linear combination on the left-hand side of (28) nor the functions $\boldsymbol{R}_{\Gamma_{T_0}} \boldsymbol{\psi}_{0,s}$, $\boldsymbol{R}_{\Gamma_{T_0}} \boldsymbol{\psi}_{1,s}$ that yield the right-hand side of (28) depend on K, while the additional constraints (29) that are due to the boundary conditions may depend explicitly on time. The time invariance of $\boldsymbol{Q}_{\Gamma_{T_0}} \boldsymbol{\psi}_{0,s}$, $\boldsymbol{Q}_{\Gamma_{T_0}} \boldsymbol{\psi}_{1,s}$ and $\boldsymbol{R}_{\Gamma_{T_0}} \boldsymbol{\psi}_{0,s}$, $\boldsymbol{R}_{\Gamma_{T_0}} \boldsymbol{\psi}_{1,s}$ is a key factor that enables the superior computational complexity of the proposed methodology, see Sections 5.3 and 5.4.

If, for a given K, the solution u needs to be known on the entire domain Ω, it can be obtained using formula (26).

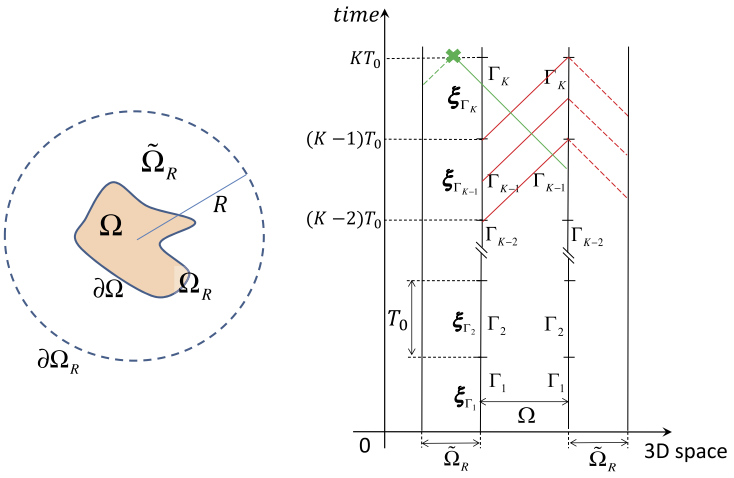

(a) Scatterer $\Omega \subset \Omega_R$; $\tilde{\Omega}_R \equiv \Omega_R \backslash \bar{\Omega}$ (b) Partition in time

Fig. 4. Geometry and partition in time for the exterior problem (30). Left panel: The larger auxiliary domain Ω_R contains Ω; the domain $\tilde{\Omega}_R$ is convenient to use for writing the Green's formula (31). Right panel: The dashed portions of the characteristic cones (shown in red) that intersect with the outer boundary of $\tilde{\Omega}_R$ correspond to the third integral in (31) that vanishes due to the radiation condition at $\partial\Omega_R \equiv \partial\tilde{\Omega}_R^{\text{out}}$. The green characteristic cone illustrates the computation of the solution in $\tilde{\Omega}$ by Calderon's potential after the boundary density has been obtained.

3. Exterior problem

A homogeneous exterior IBVP also can be reduced to an equivalent boundary formulation. Let $\Omega \subset \mathbb{R}^3$ be a bounded domain (as in Section 2), and denote its complement to the entire space by $\tilde{\Omega} \stackrel{\text{def}}{=} \mathbb{R}^3 \backslash \bar{\Omega}$. Consider the following problem [cf. equations (2)]:

$$\Box_c u(\boldsymbol{x}, t) = 0, \quad (\boldsymbol{x}, t) \in \tilde{\Omega} \times (0, T], \tag{30a}$$

$$u\big|_{t=0} = 0, \quad \frac{\partial u}{\partial t}\Big|_{t=0} = 0, \quad \boldsymbol{x} \in \tilde{\Omega}, \tag{30b}$$

$$\boldsymbol{l}_\Gamma u = \phi, \quad (\boldsymbol{x}, t) \in \Gamma \equiv \partial\tilde{\Omega} \times (0, T]. \tag{30c}$$

The boundary Γ in (30c) is clearly the same as that in (2c) since $\partial\Omega = \partial\tilde{\Omega}$. Problem (30) does not correspond to the most general exterior formulation, because both the governing equation (30a) and the initial conditions (30b) are homogeneous. Yet, this formulation is typical and important for applications. In particular, one can think of the scattering of a given incident wave about an obstacle Ω. In this case, u is the scattered field. The wave equation (30a) is homogeneous because the scattered field is not driven by any sources located on $\tilde{\Omega}$. The initial conditions (30b) are homogeneous because with no loss of generality we can assume that the incident wave only reaches the scatterer Ω at $t = 0$. The boundary operator $\boldsymbol{l}_\Gamma$ on the left-hand side of (30c) accounts for the type of scattering, while the boundary data ϕ represent the specific impinging signal. In acoustics, for example, the two most typical types of scattering surfaces are sound-soft and sound-hard. They are modeled by the Dirichlet and Neumann boundary conditions, respectively, so that relation (30c) becomes $u = -u^{\text{inc}}$ or $\frac{\partial u}{\partial \boldsymbol{n}} = -\frac{\partial u^{\text{inc}}}{\partial \boldsymbol{n}}$, where u^{inc} is the given incident field.

To reduce the exterior IBVP (30) to its boundary counterpart, consider a larger bounded domain $\Omega_R \supset \Omega$ and denote $\tilde{\Omega}_R \stackrel{\text{def}}{=} \Omega_R \backslash \bar{\Omega}$, see Fig. 4a. The boundary of the domain $\tilde{\Omega}_R$ consists of two components, inner and outer: $\partial\tilde{\Omega}_R = \partial\tilde{\Omega}_R^{\text{in}} \cup \partial\tilde{\Omega}_R^{\text{out}}$, where $\partial\tilde{\Omega}_R^{\text{in}} \equiv \partial\Omega$ and $\partial\tilde{\Omega}_R^{\text{out}} \equiv \partial\Omega_R$. As the domain $\tilde{\Omega}_R$ is finite (i.e., bounded), it allows for a convenient representation of the solution u to IBVP (30) by means of a Green's formula.

To derive the Green's formula for $\tilde{\Omega}_R$, we employ the fundamental solution (3) and, using the same argument[7] as in Section 2.1, obtain for $(\boldsymbol{x}, t) \in \tilde{\Omega}_R \times (0, T)$ [cf. formula (5)]:

$$u(\boldsymbol{x}, t) = \underbrace{\frac{1}{c^2} \int_{\tilde{\Omega}_R} \left\{ \frac{\partial u}{\partial t}(\boldsymbol{y}, 0) G(\boldsymbol{x} - \boldsymbol{y}, t) - u(\boldsymbol{y}, 0) \frac{\partial G}{\partial t}(\boldsymbol{x} - \boldsymbol{y}, t) \right\} d\boldsymbol{y}}_{=0}$$

[7] Recall, the transition from equation (4) to equation (5) in Section 2.1 was enabled by causality. Similarly, in formula (31) we have already dropped the integral over $\tilde{\Omega}_R$ at the final moment of time $t = T$ since it is zero. Moreover, the integration over the lateral boundaries is conducted only until the current moment of time t.

$$+\int_{\Gamma_t}\left\{\frac{\partial u}{\partial \boldsymbol{n}}(\boldsymbol{y},t')G(\boldsymbol{x}-\boldsymbol{y},t-t')-u(\boldsymbol{y},t')\frac{\partial G}{\partial \boldsymbol{n}}(\boldsymbol{x}-\boldsymbol{y},t-t')\right\}dt'dS_{\boldsymbol{y}} \tag{31}$$

$$+\underbrace{\int_{\Gamma_t^R}\left\{\frac{\partial u}{\partial \boldsymbol{n}}(\boldsymbol{y},t')G(\boldsymbol{x}-\boldsymbol{y},t-t')-u(\boldsymbol{y},t')\frac{\partial G}{\partial \boldsymbol{n}}(\boldsymbol{x}-\boldsymbol{y},t-t')\right\}dt'dS_{\boldsymbol{y}}}_{=0}.$$

The first integral on the right-hand side of formula (31) is zero because the initial conditions (30b) are homogeneous. The normal $\boldsymbol{n}$ in the second and third integral is considered outward with respect to $\tilde{\Omega}_R$. It means, in particular, that at the interior boundary $\partial\tilde{\Omega}_R^{\text{in}}=\partial\Omega$ its direction is opposite to that in the second integral of (5), because the outward normal with respect to $\tilde{\Omega}_R$ becomes the inward normal with respect to Ω. The third integral on the right-hand side of (31), which is taken over the outer boundary $\Gamma_t^R=\partial\tilde{\Omega}_R^{\text{out}}\times(0,t]=\partial\Omega_R\times(0,t]$, is not present at all in formula (5). For $\boldsymbol{x}\in\tilde{\Omega}_R$, we require that this integral be equal to zero.

The latter requirement means that we allow no incoming waves through the outer boundary Γ_t^R, i.e., that no information may propagate from the boundary Γ_t^R inwards and affect the solution u inside $\tilde{\Omega}_R$, see Fig. 4b. For convex boundary shapes $\partial\Omega_R$, this is equivalent to having a perfectly non-reflecting boundary Γ_t^R (see, e.g., [41]). In Fig. 4a, the boundary $\partial\Omega_R$ is shown as spherical for simplicity, yet other convex boundaries can be used as well.

In fact, the outer boundary $\partial\Omega_R$ is artificial; its key role is to help us write the Green's formula on a bounded domain. Yet a perfect ABC at $\partial\Omega_R$ that guarantees the non-reflectioning radiation of waves automatically implies that on the right-hand side of (31) there will be only one non-vanishing term — the second integral, which is taken over the interior boundary $\Gamma_t=\partial\tilde{\Omega}_R^{\text{in}}\times(0,t]$, see Fig. 4. This is a manifestation of the fact that the scattered (outgoing) field governed by the homogeneous wave equation (30a) is determined solely by its trace at the boundary of the scatterer. Hence, we can formally extend the Green's formula (31) beyond $\tilde{\Omega}_R$ — to all $\boldsymbol{x}\in\tilde{\Omega}$.

The Calderon's potential for the exterior problem is given by [cf. formula (6)]:

$$\boldsymbol{P}_{\tilde{\Omega}}\boldsymbol{\xi}_{\Gamma_t}(\boldsymbol{x},t)=\int_{\Gamma_t}\left\{\xi_1(\boldsymbol{y},t')G(\boldsymbol{x}-\boldsymbol{y},t-t')-\xi_0(\boldsymbol{y},t')\frac{\partial G}{\partial \boldsymbol{n}}(\boldsymbol{x}-\boldsymbol{y},t-t')\right\}dt'dS_{\boldsymbol{y}},\quad \boldsymbol{x}\in\tilde{\Omega}. \tag{32}$$

The density $\boldsymbol{\xi}_{\Gamma_t}=(\xi_0,\xi_1)$ of the potential (32) is defined on the same space–time boundary Γ_t as that for the interior problem. Similarly to (9) and (7), the boundary projection is defined as the trace of the potential (32): $\boldsymbol{P}_{\Gamma_t}\overset{\text{def}}{=}\boldsymbol{Tr}_{\Gamma_t}\boldsymbol{P}_{\tilde{\Omega}}$, and the boundary equation with projection for the exterior problem reads [cf. equation (10)]:

$$\boldsymbol{P}_{\Gamma_t}\boldsymbol{\xi}_{\Gamma_t}=\boldsymbol{\xi}_{\Gamma_t}. \tag{33}$$

Similarly to in the case of interior problems, the BEP (33) holds if and only if the density $\boldsymbol{\xi}_{\Gamma_t}=(\xi_0,\xi_1)$ coincides with the trace of a solution to the homogeneous wave equation (30a) on $\tilde{\Omega}$ subject to the homogeneous initial conditions (30b). Since in the case of exterior problems the initial conditions are always assumed homogeneous, we need not consider the inhomogeneous BEPs of type (10′). To obtain the solution to the full IBVP (30), one needs to supplement the BEP (33) with the boundary condition (30c).

The solution algorithm for system (33), (30c) over the interval $0\leqslant t\leqslant T$ is basically the same as that for the interior problem. It involves the partition in time of the boundary Γ_T and the density $\boldsymbol{\xi}_{\Gamma_T}$, see formulae (12), (13), (14) and Fig. 4b. The partial densities are updated sequentially [cf. equation (25)]:

$$\boldsymbol{P}_{\Gamma_{T_0}}\boldsymbol{\xi}_{\Gamma_K}+\boldsymbol{R}_{\Gamma_{T_0}}\boldsymbol{\xi}_{\Gamma_{K-1}}=\boldsymbol{\xi}_{\Gamma_K}, \tag{34}$$

where $\boldsymbol{P}_{\Gamma_{T_0}}=\boldsymbol{Tr}_{\Gamma_{T_0}}\boldsymbol{P}_{\tilde{\Omega}}$ and the operator $\boldsymbol{R}_{\Gamma_{T_0}}$ is defined similarly to (24) (only the direction of $\boldsymbol{n}$ is opposite):

$$\boldsymbol{R}_{\Gamma_{T_0}}\boldsymbol{\xi}_{\Gamma_{K-1}}(\boldsymbol{x},t)=\boldsymbol{Tr}_{\Gamma_K}\int_{T-2T_0}^{T-T_0}\left\{\xi_1(\boldsymbol{y},t')G(\boldsymbol{x}-\boldsymbol{y},t-t')-\xi_0(\boldsymbol{y},t')\frac{\partial G}{\partial \boldsymbol{n}}(\boldsymbol{x}-\boldsymbol{y},t-t')\right\}dt'dS_{\boldsymbol{y}},$$

$$\boldsymbol{x}\in\partial\Omega,\quad T-T_0<t\leqslant T.$$

Neither of the two operators, $\boldsymbol{P}_{\Gamma_{T_0}}$ or $\boldsymbol{R}_{\Gamma_{T_0}}$, depends on K, i.e., both admit translation in time, see Sections 2.2 and 2.3. The sequential update based on equation (34) supplemented by (22) is enabled by the Huygens' principle, specifically, by the lacuna of the fundamental solution (3). The semi-discretization described in Section 2.4, as well as the solution procedure with respect to the unknown expansion coefficients $c_{0,s}^{(\text{II})}$, $c_{1,s}^{(\text{II})}$, apply to exterior problems with no modifications.

An important difference between the interior and exterior formulation arises at the final stage of the algorithm where the solution on the domain of interest (not only at the boundary) is computed with the help of the Calderon's potential. For an interior problem, it is sufficient to know only the immediately preceding partial density $\boldsymbol{\xi}_{\Gamma_K}$ to obtain the solution

on the entire domain Ω at $t = T$, see formula (26). For an exterior problem, however, one needs both $\boldsymbol{\xi}_{\Gamma_K}$ and $\boldsymbol{\xi}_{\Gamma_{K-1}}$ to compute $u(\boldsymbol{x}, T)$ for the locations $\boldsymbol{x}$ that are no further away from Ω than $\operatorname{diam}\Omega$:

$$u(\boldsymbol{x}, T) = \boldsymbol{P}_{\tilde{\Omega}}\boldsymbol{\xi}_{\Gamma_K} + \boldsymbol{P}_{\tilde{\Omega}}\boldsymbol{\xi}_{\Gamma_{K-1}}, \quad \operatorname{dist}(\boldsymbol{x}, \Omega) \leqslant \operatorname{diam}\Omega.$$

This situation is illustrated in Fig. 4b: the green characteristic cone with the vertex in $\tilde{\Omega}_R$ at $t = T$ intersects Γ_K and Γ_{K-1}. For even more "remote" points $\boldsymbol{x}$ one would, generally speaking, need additional partial densities: $\boldsymbol{\xi}_{\Gamma_{K-2}}$, $\boldsymbol{\xi}_{\Gamma_{K-3}}$, ... It means that whereas the boundary time-marching algorithm with respect to K still involves only two consecutive partial densities, see formulae (34), (22), for computing the solution on the exterior domain one should store the previous densities as well. While technically speaking this is unavoidable if the solution is to be known far away from the scatterer, we emphasize that in many applications it is not required. For example, for computing scattering cross-sections, only the near field of the scatterer needs to be available.

4. The method of difference potentials

In this section, we introduce a fully discrete formulation of the problem based on boundary equations with projections. It involves the discretization and numerical solution of the boundary equations (28)–(29) by the method of difference potentials. For definiteness, we discuss only the interior problems of Section 2. The discretization of exterior problems (Section 3) will be presented in a subsequent work. In what follows, we will not provide a comprehensive account of the method of difference potentials, as its detailed exposition is available in the literature [4]. The purpose of this section is rather to outline the key components of the MDP for time-dependent problems, as opposed to steady-state or time-harmonic problems that it has been applied to previously (see, e.g., the recent publications [36,37]). We begin with presenting an alternative yet equivalent definition of Calderon's potentials that will be more convenient for numerical implementation, see Section 4.1.

4.1. Auxiliary problem

Let $\boldsymbol{\xi}_{\Gamma_t} = (\xi_0, \xi_1)$ be given, and let $w = w(\boldsymbol{x}, t)$ be an arbitrary sufficiently smooth function that is compactly supported in space and satisfies $\boldsymbol{Tr}_{\Gamma_t} w = \boldsymbol{\xi}_{\Gamma_t}$, where the operator $\boldsymbol{Tr}_{\Gamma_t}$ is defined by (7). Generally speaking, $\Box_c w \neq 0$. Therefore, for $\boldsymbol{x} \in \Omega$ the Green's formula (5) generalizes to

$$\begin{aligned} w(\boldsymbol{x}, t) = {} & \frac{1}{c^2}\int\limits_{\Omega}\left\{\frac{\partial w}{\partial t}(\boldsymbol{y}, 0)G(\boldsymbol{x}-\boldsymbol{y}, t) - w(\boldsymbol{y}, 0)\frac{\partial G}{\partial t}(\boldsymbol{x}-\boldsymbol{y}, t)\right\}d\boldsymbol{y} \\ & + \int\limits_{\Gamma_t}\left\{\frac{\partial w}{\partial \boldsymbol{n}}(\boldsymbol{y}, t')G(\boldsymbol{x}-\boldsymbol{y}, t-t') - w(\boldsymbol{y}, t')\frac{\partial G}{\partial \boldsymbol{n}}(\boldsymbol{x}-\boldsymbol{y}, t-t')\right\}dt'dS_{\boldsymbol{y}} \\ & + \int\limits_0^t\int\limits_{\Omega} G(\boldsymbol{x}-\boldsymbol{y}, t-t')\Box_c w(\boldsymbol{y}, t')d\boldsymbol{y}dt', \end{aligned} \tag{35}$$

see [40, equation (7.3.5)]. Since $\boldsymbol{Tr}_{\Gamma_t} w = \boldsymbol{\xi}_{\Gamma_t}$, the second integral on the right-hand side of (35) coincides with the second integral on the right-hand side of (6). Consequently, for Calderon's potential with the density $\boldsymbol{\xi}_{\Gamma_t}$ we can write:

$$\begin{aligned} \boldsymbol{P}_{\Omega}\boldsymbol{\xi}_{\Gamma_t}(\boldsymbol{x}, t) = w(\boldsymbol{x}, t) & - \int\limits_0^t\int\limits_{\Omega} G(\boldsymbol{x}-\boldsymbol{y}, t-t')\Box_c w(\boldsymbol{y}, t')d\boldsymbol{y}dt' \\ & - \frac{1}{c^2}\int\limits_{\Omega}\left\{\frac{\partial w}{\partial t}(\boldsymbol{y}, 0)G(\boldsymbol{x}-\boldsymbol{y}, t) - w(\boldsymbol{y}, 0)\frac{\partial G}{\partial t}(\boldsymbol{x}-\boldsymbol{y}, t)\right\}d\boldsymbol{y}, \end{aligned} \tag{36}$$

where it is assumed that $\boldsymbol{x} \in \Omega$ and $t > 0$. Let us introduce the following new notations:

$$\begin{aligned} f(\boldsymbol{x}, t) &\stackrel{\text{def}}{=} \begin{cases} \Box_c w(\boldsymbol{x}, t), & \text{if } \boldsymbol{x} \in \Omega, \\ 0, & \text{elsewhere}, \end{cases} \\ w_0(\boldsymbol{x}) &\stackrel{\text{def}}{=} \begin{cases} w(\boldsymbol{x}, 0), & \text{if } \boldsymbol{x} \in \Omega, \\ 0, & \text{elsewhere}, \end{cases} \\ w_1(\boldsymbol{x}) &\stackrel{\text{def}}{=} \begin{cases} \frac{\partial w}{\partial t}(\boldsymbol{x}, 0), & \text{if } \boldsymbol{x} \in \Omega, \\ 0, & \text{elsewhere}. \end{cases} \end{aligned} \tag{37}$$

Using (37), we can recast equation (36) as

$$\begin{aligned}\boldsymbol{P}_{\Omega}\boldsymbol{\xi}_{\Gamma_t}(\boldsymbol{x},t) = w(\boldsymbol{x},t) - \int_0^t \int_{\mathbb{R}^3} G(\boldsymbol{x}-\boldsymbol{y},t-t')f(\boldsymbol{y},t')d\boldsymbol{y}dt' \\ -\frac{1}{c^2}\int_{\mathbb{R}^3}\left\{w_1(\boldsymbol{y})G(\boldsymbol{x}-\boldsymbol{y},t) - w_0(\boldsymbol{y})\frac{\partial G}{\partial t}(\boldsymbol{x}-\boldsymbol{y},t)\right\}d\boldsymbol{y},\end{aligned} \tag{36'}$$

where the key difference between (36) and (36′) is that the spatial integration in (36′) is formally conducted over the entire $\mathbb{R}^3$ rather than over Ω. Then, it is easy to see that the second and third terms on the right-hand side of (36′) represent the solution to the following Cauchy problem:

$$\Box_c v(\boldsymbol{x},t) = f(\boldsymbol{x},t), \quad \boldsymbol{x}\in\mathbb{R}^3,\ t>0, \tag{38a}$$

$$v\big|_{t=0} = w_0, \quad \frac{\partial v}{\partial t}\Big|_{t=0} = w_1, \quad \boldsymbol{x}\in\mathbb{R}^3. \tag{38b}$$

Hereafter, problem (38) will be referred to as the auxiliary problem (AP). It will be convenient to use a compact notation for the solution of the AP:

$$v = \boldsymbol{G}(f, w_0, w_1) = \boldsymbol{G}\big(\Box_c w\big|_{\Omega}, w_0, w_1\big),$$

where $\boldsymbol{G}$ is the inverse operator given by the two integrals on the right-hand side of (36′). Then,

$$\boldsymbol{P}_{\Omega}\boldsymbol{\xi}_{\Gamma_t}(\boldsymbol{x},t) = w(\boldsymbol{x},t) - \boldsymbol{G}\big(\Box_c w\big|_{\Omega}, w_0, w_1\big), \quad \boldsymbol{x}\in\Omega. \tag{36''}$$

By design, the Calderon's potential $\boldsymbol{P}_{\Omega}\boldsymbol{\xi}_{\Gamma_t}(\boldsymbol{x},t)$ of (36″), where $\boldsymbol{G}$ is the inverse operator of the AP (38), does not depend on the choice of the auxiliary function w as long as $\boldsymbol{Tr}_{\Gamma_t} w = \boldsymbol{\xi}_{\Gamma_t}$.

4.2. Discrete AP

The AP (38) is a Cauchy problem formulated on an unbounded region — the entire $\mathbb{R}^3$. According to (37), its right-hand side and the initial data are compactly supported in space on the domain Ω. Since the propagation speed c is finite, it is clear that by the time $T>0$ no wave can travel further away from Ω than the distance cT. Hence, as there are no sources of the field outside Ω, the solution of the AP beyond the aforementioned distance will be equal to zero. Consequently, for a given final time T the computational domain for the Cauchy problem (38) can be terminated by a zero boundary condition at the distance cT from Ω. This is the most straightforward approach to truncating the original unbounded domain of problem (38).

Denote by Ω_0 the resulting bounded auxiliary domain beyond which the solution of the AP (38) is zero on the interval $0<t\leqslant T$. On the domain Ω_0, the AP can be discretized using any appropriate finite difference scheme and supplemented by zero boundary conditions at $\partial\Omega_0$. In this work, we employ the most common central difference second order accurate scheme on a uniform Cartesian mesh with size h in space; the scheme is stable provided that its time step τ satisfies the standard CFL condition: $\tau\leqslant h/c\sqrt{3}$. In doing so, the auxiliary domain Ω_0 can have a simple shape suggested by the discretization, e.g., it can be a cube. The actual boundary $\partial\Omega$ does not have to conform to the discretization grid; this is one of the key advantages of the MDP.

We will use the superscript "(h)" to denote the discrete functions and operators. Then, for the solution of the difference AP we can write:

$$v^{(h)} = \boldsymbol{G}^{(h)}(f^{(h)}, w_0^{(h)}, w_1^{(h)}),$$

where $f^{(h)}$ is the discrete right-hand side on the grid, and $w_0^{(h)}$ and $w_1^{(h)}$ are the initial data. The latter, unlike in Section 4.1, are interpreted as the values of the solution on the first two time levels. Note, that high order accurate schemes are beneficial as they reduce the numerical dispersion; later, we will incorporate the compact fourth order accurate scheme [35] into our algorithm.

As we have seen, the size of the auxiliary domain Ω_0 is determined by Ω and the final time T. It is very important that the time T for the AP never needs to be large, even though the overall simulation time may be arbitrarily long. Indeed, the Huygens' principle that our methodology relies on allows us to take $T=2T_0$, because having the solution of the AP (38) on Ω for $0<t\leqslant 2T_0$ is sufficient for obtaining the operators $\boldsymbol{P}_{\Gamma_{T_0}}$ and $\boldsymbol{R}_{\Gamma_{T_0}}$ in equation (25). Moreover, the "spare" distance $cT=2cT_0$ required for solving the AP can, in fact, be halved, i.e., reduced to cT_0. To see that, let $\Omega_0\supset\Omega$ be such that $\mathrm{dist}(\partial\Omega_0,\Omega)\gtrsim cT_0$. We can set an arbitrary (well-posed) boundary condition at $\partial\Omega_0\times(0,2T_0]$. Then, no wave reflected from this artificial outer boundary and traveling back toward Ω will be able to reach Ω before the computation is terminated at $T=2T_0$. Consequently, the solution inside Ω for $0<t\leqslant 2T_0$ will remain exactly the same as the solution to the genuine

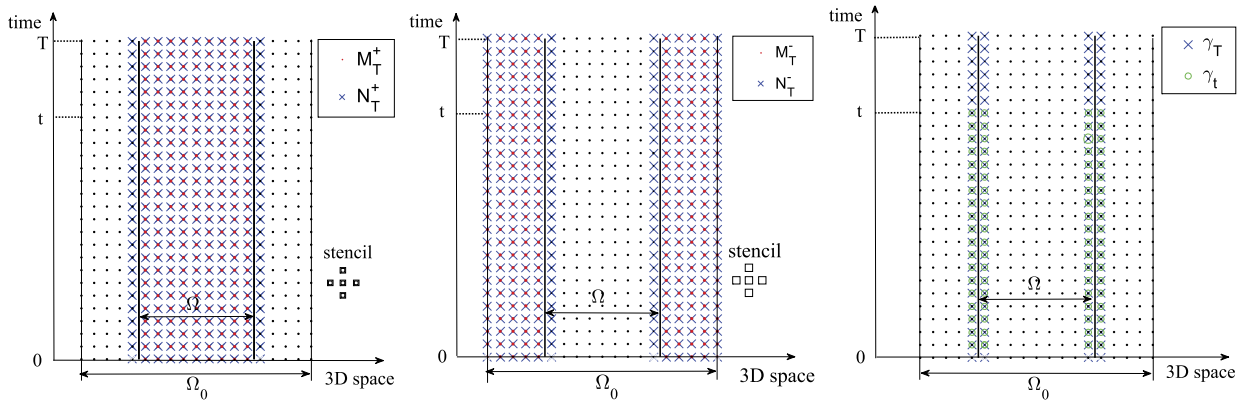

(a) $\mathbb{M}_T^+$ and $\mathbb{N}_T^+$ (b) $\mathbb{M}_T^-$ and $\mathbb{N}_T^-$ (c) γ_T and γ_t

Fig. 5. One-dimensional schematic for the grid sets.

Cauchy problem (38). We have used this approach extensively to design the lacunae-based artificial boundary conditions (ABCs) for wave propagation problems [27–29]. In the current paper, we will be using it for the numerical simulations of Section 5. Other useful techniques for truncating the domain of the AP include ABCs, as well as perfectly matched layers (PMLs), at $\partial\Omega_0$. In particular, a PML has been used for the computations reported in Section 5.4. Further discussion on the treatment of outer boundaries for the AP is presented in Section 6.

4.3. Grid sets

Denote by $\mathbb{N}_T^0$ the space–time discretization grid on which the solution to the finite difference AP is defined, so that for the entire solution we have $v^{(h)} \equiv v^{(h)}_{\mathbb{N}_T^0}$. The grid $\mathbb{N}_T^0$ occupies the auxiliary domain $\Omega_0 \times [0, T]$ introduced in Section 4.2. Likewise, let $\mathbb{M}_T^0$ be the grid, on which the discrete right-hand side $f^{(h)} \equiv f^{(h)}_{\mathbb{M}_T^0}$ is defined. In the case of a central difference Cartesian discretization employed in the current paper, the nodes of the two grids coincide and we make a distinction between them only for the purpose of considering $v^{(h)}$ and $f^{(h)}$ separately. However, for a different scheme, e.g., staggered, $\mathbb{N}_T^0$ and $\mathbb{M}_T^0$ may actually be two different grids. For building the difference potentials, the various subsets of the grids $\mathbb{N}_T^0$ and $\mathbb{M}_T^0$ are of central importance.

Define $\mathbb{M}_T^+ = \mathbb{M}_T^0 \cap \{\Omega \times [0, T]\}$ and $\mathbb{M}_T^- = \mathbb{M}_T^0 \setminus \mathbb{M}_T^+$. In other words, the set $\mathbb{M}_T^+$ contains all the nodes of the spade-time grid $\mathbb{M}_T^0$ that happen to be inside $\Omega \times [0, T]$ (i.e., interior nodes), while $\mathbb{M}_T^-$ is the complement of $\mathbb{M}_T^+$ to the entire $\mathbb{M}_T^0$. The right-hand side $f^{(h)}$ will be non-zero on $\mathbb{M}_T^+$ and zero on $\mathbb{M}_T^-$. Let $\mathbb{N}_m$ be the space–time stencil of the scheme centered at a given node $m \in \mathbb{M}_T^0$.[8] Introduce the sets

$$\mathbb{N}_T^+ = \bigcup_{m \in \mathbb{M}_T^+} \mathbb{N}_m, \qquad \mathbb{N}_T^- = \bigcup_{m \in \mathbb{M}_T^-} \mathbb{N}_m, \quad \text{and} \quad \gamma_T = \mathbb{N}_T^+ \cap \mathbb{N}_T^-.$$

The set γ_T is called the grid boundary. It is a fringe of nodes that straddles the continuous boundary Γ_T. Clearly, similar grid sets can be defined for any $t < T$. In particular, we will be using the grid boundary γ_t hereafter. It can be thought of as a discrete counterpart of Γ_t (see Section 2.1). Figs. 5 and 6 schematically illustrate the foregoing grid sets.

4.4. Difference potentials

Let ξ_{γ_t} be a scalar grid function defined at the grid boundary γ_t, see Fig. 5c. Let $w^{(h)}$ be an auxiliary grid function defined on $\mathbb{N}_t^0$ such that its trace on γ_t coincides with ξ_{γ_t}:

$$\boldsymbol{Tr}^{(h)}_{\gamma_t} w^{(h)} = \xi_{\gamma_t}.$$

The discrete trace operator $\boldsymbol{Tr}^{(h)}_{\gamma_t}$ restricts the grid function that it operates on from a larger set $\mathbb{N}_t^0$ to the smaller set $\gamma_t \subset \mathbb{N}_t^0$. Denote by $\Box_c^{(h)}$ the central difference discretization of the d'Alembert operator and define [cf. formulae (37)]:

[8] To allow the stencil $\mathbb{N}_m$ to apply to every node of $\mathbb{M}_T^0$, the grid $\mathbb{N}_T^0$ must have one additional layer of nodes at the boundaries of Ω_0, as well as at the initial and final moments of time.

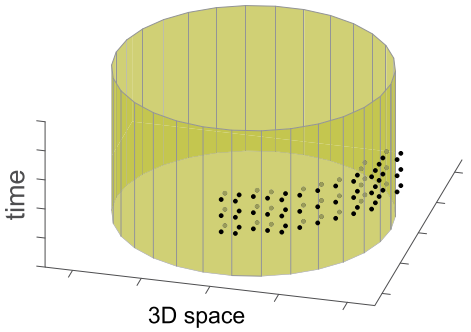

Fig. 6. Two-dimensional schematic for a fragment of the set γ_T.

$$
\begin{aligned}
f^{(h)}_{M^0_t}\big|_m &\stackrel{\text{def}}{=} \begin{cases} \square^{(h)}_c w^{(h)}, & \text{if } m \in \mathbb{M}^+_t, \\ 0, & \text{if } m \in \mathbb{M}^-_t, \end{cases} \\
w^{(h)}_0\big|_n &\stackrel{\text{def}}{=} \begin{cases} w^{(h)}\big|_{n_0=0}, & \text{if } n \in \mathbb{N}^+_t, \\ 0, & \text{if } n \notin \mathbb{N}^+_t, \end{cases} \\
w^{(h)}_1\big|_n &\stackrel{\text{def}}{=} \begin{cases} w^{(h)}\big|_{n_0=1}, & \text{if } n \in \mathbb{N}^+_t, \\ 0, & \text{if } n \notin \mathbb{N}^+_t, \end{cases}
\end{aligned}
\tag{39}
$$

where the first component n_0 of the four-dimensional multi-index $n = (n_0, n_1, n_2, n_3)$ is assumed to correspond to the time variable. Thus, the second and third equations of (39) define the initial data at the first two time levels of the discretization grid.

The difference potential with the density ξ_{γ_t} is a grid function defined on $\mathbb{N}^+_t$ [cf. formula (36″)]:

$$
\boldsymbol{P}_{\mathbb{N}^+_t}\xi_{\gamma_t} = w^{(h)}\big|_{\mathbb{N}^+_t} - \boldsymbol{G}^{(h)}\big(f^{(h)}_{M^0_t}, w^{(h)}_0, w^{(h)}_1\big), \tag{40}
$$

where the source terms for the difference AP are given by formulae (39). As $w^{(h)} = \boldsymbol{G}^{(h)}\square^{(h)}_c w^{(h)}$, the difference potential (40) satisfies the homogeneous finite difference d'Alembert equation on $\mathbb{M}^+_t$:

$$
\square^{(h)}_c \boldsymbol{P}_{\mathbb{N}^+_t}\xi_{\gamma_t}\Big|_{\mathbb{M}^+_t} = 0.
$$

The difference boundary projection is obtained by restricting the potential (40) to the grid boundary γ_t [cf. formula (9)]:

$$
\boldsymbol{P}_{\gamma_t}\xi_{\gamma_t} \stackrel{\text{def}}{=} \boldsymbol{Tr}^{(h)}_{\gamma_t}\boldsymbol{P}_{\mathbb{N}^+_t}\xi_{\gamma_t}. \tag{41}
$$

By design, neither the difference potential (40) nor the difference projection (41) depend on the choice of the auxiliary function $w^{(h)}$ as long as the latter satisfies $\boldsymbol{Tr}^{(h)}_{\gamma_t} w^{(h)} = \xi_{\gamma_t}$.

The homogeneous finite difference BEP [cf. equation (10)]

$$
\boldsymbol{P}_{\gamma_t}\xi_{\gamma_t} = \xi_{\gamma_t} \tag{42}
$$

holds if and only if $\xi_{\gamma_t} = \boldsymbol{Tr}^{(h)}_{\gamma_t} u^{(h)}_{\mathbb{N}^+_t}$, where $u^{(h)}_{\mathbb{N}^+_t}$ is a grid function that solves the homogeneous difference wave equation: $\square^{(h)}_c u^{(h)}_{\mathbb{N}^+_t}\big|_{\mathbb{M}^+_t} = 0$, and satisfies zero initial conditions. The inhomogeneous finite difference BEP [cf. equation (10′)]

$$
\boldsymbol{P}_{\gamma_t}\xi_{\gamma_t} + \boldsymbol{Tr}^{(h)}_{\gamma_t}\boldsymbol{G}^{(h)}\big(0, u^{(h)}_0, u^{(h)}_1\big) = \xi_{\gamma_t} \tag{42′}
$$

holds if and only if $\exists u^{(h)}_{\mathbb{N}^+_t}$ such that $\boldsymbol{Tr}^{(h)}_{\gamma_t} u^{(h)}_{\mathbb{N}^+_t} = \xi_{\gamma_t}$, $\square^{(h)}_c u^{(h)}_{\mathbb{N}^+_t}\big|_{\mathbb{M}^+_t} = 0$, and the initial values of $u^{(h)}_{\mathbb{N}^+_t}$ are $u^{(h)}_0$ and $u^{(h)}_1$. Thus, the discrete BEP equivalently reduces the finite difference wave equation $\square^{(h)}_c u^{(h)}_{\mathbb{N}^+_t}\big|_{\mathbb{M}^+_t} = 0$ (subject to homogeneous initial conditions in the case (42) or inhomogeneous initial conditions in the case (42′)) from the grid $\mathbb{N}^+_t$ to the grid boundary γ_t. This is similar to the continuous setting of Section 2.1, where the BEP (10) (homogeneous) or (10′) (inhomogeneous) reduce the d'Alembert equation (2a) from the domain $\Omega \times (0, t]$ to the boundary Γ_t.

There are many functions ξ_{γ_t} that satisfy the discrete BEP (42) or (42′), just as there are many functions $u^{(h)}_{\mathbb{N}^+_t}$ that solve the discrete d'Alembert equation $\square^{(h)}_c u^{(h)}_{\mathbb{N}^+_t}$ on the interior nodes $\mathbb{M}^+_t$ (and satisfy the appropriate initial conditions). To make

the BEP uniquely solvable, we must account for the boundary condition (11) on Γ_t. However, the discrete BEP is enforced at the grid boundary γ_t rather than on the continuous boundary Γ_t. We merge the two formulations by expanding the boundary data with respect to the same finite set of basis functions as in Section 2.4, and then applying the equation-based extension.

Consider the vector-valued function $\boldsymbol{\xi}_{\Gamma_t} = (\xi_0, \xi_1)\big|_{\Gamma_t}$ that represents the trace of the solution u to the wave equation (2a) and its outward normal derivative $\frac{\partial u}{\partial \boldsymbol{n}}$ on the boundary. Given the density $\boldsymbol{\xi}_\Gamma$, the extension defines an approximation $\boldsymbol{Ex}\boldsymbol{\xi}_\Gamma$ of u at the discrete boundary γ_t. It is the extension $\boldsymbol{Ex}\boldsymbol{\xi}_\Gamma$ that takes the place of ξ_{γ_t} in the difference BEP.

To have the boundary time-marching scheme of Section 2.3 implemented in a fully discrete setting, we will use the appropriate difference counterparts of the operators $\boldsymbol{P}_{\Gamma_{T_0}}$ and $\boldsymbol{R}_{\Gamma_{T_0}}$ in equation (25). The discrete analogue of the continuous projection $\boldsymbol{P}_{\Gamma_{T_0}}$ is $\boldsymbol{P}_{\gamma_{T_0}} \equiv \boldsymbol{P}_{\gamma_t}\big|_{t=T_0}$ obtained by formula (41). The discrete analogue of $\boldsymbol{R}_{\Gamma_{T_0}}$, which we denote $\boldsymbol{R}_{\gamma_{T_0}}$, is also defined as the trace of a difference potential, but similarly to (24):

$$\boldsymbol{R}_{\gamma_{T_0}} \xi_{\gamma_{T_0}} \stackrel{\text{def}}{=} \boldsymbol{Tr}^{(h)}_{\gamma_{(T_0,2T_0]}} \boldsymbol{P}_{\mathbb{N}^+_{2T_0}} \xi_{\gamma_{T_0}}. \tag{43}$$

While the argument of $\boldsymbol{R}_{\gamma_{T_0}}$, i.e., the density $\xi_{\gamma_{T_0}}$, is specified for $0 < t \leqslant T_0$, the difference potential with this density is computed on the time interval of twice the duration: $0 < t \leqslant 2T_0$, and the boundary trace, which yields the result of application of the operator $\boldsymbol{R}_{\gamma_{T_0}}$ to $\xi_{\gamma_{T_0}}$, is taken at the upper portion of the grid boundary: $\gamma_{(T_0,2T_0]} = \gamma_{2T_0} \setminus \gamma_{T_0}$. By design, the grid sets γ_{T_0} and $\gamma_{(T_0,2T_0]}$ are identical yet shifted in time with respect to one another.

4.5. Equation-based extension

The difference potential may approximate the corresponding continuous Calderon's potential provided that a certain relation holds between their respective densities. This relation is given by the equation-based extension that we introduce in the current section. Let $\boldsymbol{\xi}_{\Gamma_t} = (\xi_0, \xi_1)\big|_{\Gamma_t}$ be given. In the vicinity of the boundary Γ_t, we introduce a new function $v = v(\boldsymbol{x}, t)$ by means of a truncated Taylor series:

$$v(\boldsymbol{x}, t) = \sum_{p=0}^{P} \frac{1}{l!} \frac{\partial^p v}{\partial \boldsymbol{n}^p}(\boldsymbol{x}_0, t) \rho^p, \tag{44}$$

where the choice of P is discussed later. In formula (44), $\boldsymbol{x} \in \mathbb{R}^3$ is a point near $\partial\Omega$ and $\boldsymbol{x}_0$ is the foot of the normal dropped from $\boldsymbol{x}$ to $\partial\Omega$. The quantity ρ is a signed distance from $\boldsymbol{x}$ to $\partial\Omega$, i.e., $\rho = |\boldsymbol{x} - \boldsymbol{x}_0|$ if $\boldsymbol{x} \notin \Omega$ and $\rho = -|\boldsymbol{x} - \boldsymbol{x}_0|$ if $\boldsymbol{x} \in \Omega$ (recall, $\boldsymbol{n}$ is the outward normal).

The derivatives on the right-hand side of (44) are defined as follows. For $p = 0$, we take $v(\boldsymbol{x}_0, t) = \xi_0(\boldsymbol{x}_0, t)$. For $p = 1$, we choose $\frac{\partial v}{\partial \boldsymbol{n}}(\boldsymbol{x}_0, t) = \xi_1(\boldsymbol{x}_0, t)$. This means that $\boldsymbol{Tr}_{\Gamma_t} v = \boldsymbol{\xi}_{\Gamma_t}$. The higher-order derivatives are obtained by employing the d'Alembert equation (2a). Namely, assuming that $\partial\Omega$ is sufficiently smooth, we can introduce local orthogonal coordinates in $\mathbb{R}^3$ such that two of the three coordinate directions will be tangential to the surface $\partial\Omega$ and the third one will be normal. Then, for the Laplacian of v on the surface we can write: $\Delta v = \frac{\partial^2 v}{\partial \boldsymbol{n}^2} + \boldsymbol{L}v$, where the operator $\boldsymbol{L}$ involves the derivatives with respect to $\boldsymbol{n}$ of the order no higher than first, as well as the tangential derivatives. For example, if $\partial\Omega$ is a sphere, then we can use spherical coordinates and write:

$$\Delta v = \frac{\partial^2 v}{\partial r^2} + \underbrace{\frac{2}{r}\frac{\partial v}{\partial r} + \frac{1}{r^2 \sin\theta}\frac{\partial}{\partial \theta}\left(\sin\theta \frac{\partial v}{\partial \theta}\right) + \frac{1}{r^2 \sin^2\theta}\frac{\partial^2 v}{\partial \varphi^2}}_{\boldsymbol{L}v}.$$

Consequently, using $\Box_c v = \frac{1}{c^2}\frac{\partial^2 v}{\partial t^2} - \Delta v = 0$, for the term with $p = 2$ in the sum (44) we obtain:

$$\frac{\partial^2 v}{\partial \boldsymbol{n}^2}(\boldsymbol{x}_0, t) = \frac{1}{c^2}\frac{\partial^2 v}{\partial t^2}(\boldsymbol{x}_0, t) - \boldsymbol{L}v(\boldsymbol{x}_0, t). \tag{45}$$

On the right-hand side of (45) we have at most first order derivatives with respect to $\boldsymbol{n}$. So we can immediately evaluate this right-hand side by substituting ξ_0 and ξ_1 in the capacity of v and $\frac{\partial v}{\partial \boldsymbol{n}}$ on the surface. In particular, $\frac{1}{c^2}\frac{\partial^2 v}{\partial t^2}(\boldsymbol{x}_0, t) = \frac{1}{c^2}\frac{\partial^2 \xi_0}{\partial t^2}(\boldsymbol{x}_0, t)$. Normal derivatives of v of orders $p > 2$ can be obtained by consecutively differentiating relation (45) with respect to $\boldsymbol{n}$ and recursively employing the d'Alembert equation to replace the arising second order derivatives on the right-hand side. This process is known as equation-based differentiation, and the resulting function $v(\boldsymbol{x}, t)$ defined by formula (44) is called the equation-based extension of the boundary data $\boldsymbol{\xi}_{\Gamma_t}$.

If $\boldsymbol{\xi}_{\Gamma_t}$ happens to be the boundary trace of a true solution to the d'Alembert equation, i.e., if $\exists u = u(\boldsymbol{x}, t)$ such that $\Box_c u = 0$ and $\boldsymbol{Tr}_{\Gamma_t} u = \boldsymbol{\xi}_{\Gamma_t}$, then the equation-based extension $v(\boldsymbol{x}, t)$ given by (44) approximates $u(\boldsymbol{x}, t)$ with accuracy $\mathcal{O}(|\rho|^{P+1})$. The extension, however, can formally be applied to an arbitrary pair of functions $\boldsymbol{\xi}_{\Gamma_t} = (\xi_0, \xi_1)\big|_{\Gamma_t}$ that do not necessarily correspond to the trace of a solution to the wave equation. In that case, it defines a new function.

In the context of the DPM, we will need to evaluate the extension (44) at the nodes of the grid boundary γ_t, which are located close to Γ_t by construction. In this case, we will write:

$$\xi_{\gamma_t} = \boldsymbol{Ex}\boldsymbol{\xi}_{\Gamma_t}, \tag{46}$$

where $\boldsymbol{Ex}$ is the extension operator (44)–(45). For elliptic equations, a judiciously chosen order P of the truncated Taylor series (44) guarantees that the difference potential with density ξ_γ will approximate the continuous Calderon's potential with density $\boldsymbol{\xi}_\Gamma$ to the design order of accuracy of the scheme,[9] see [42]. In [36], we have shown that it is sufficient to take $P = 4$ to achieve fourth order accuracy for the Helmholtz equation. Earlier it has been shown that for second order accuracy one can take $P = 2$. The analysis of [42] has not been generalized to the case of hyperbolic equations (yet). Therefore, in the current paper we take the order P the same as we would have taken it in the elliptic case, and then verify the grid convergence experimentally, see Section 5.2. Specifically, as the scheme introduced in Section 4.2 is second order accurate, we choose $P = 2$.

4.6. Full discretization

The discretization that we obtain by means of the MDP employs the discrete BEPs (42), (42′) with the difference projection $\boldsymbol{P}_{\gamma_t}$ that acts on the functions at the grid boundary γ_t. The unknowns remain defined at the continuous boundary Γ_t. The two boundaries are connected via the equation-based extension described in Section 4.5. This extension facilitates the approximation of the continuous potentials by difference potentials.

The time-marching algorithm of Section 2.4 operates with the partition elements of duration $t = T_0$ (implication of the Huygens' principle). To represent the solution at the continuous boundary $\Gamma_t = \Gamma_{T_0}$, we employ the basis introduced in Section 2.4. In the numerical simulations of Section 5, the boundary $\partial\Omega$ is spherical. Hence, we take the individual basis functions ψ_s as products of spherical harmonics on the surface $\partial\Omega$ times Chebyshev polynomials in time. For other shapes of $\partial\Omega$, one can use some other type of spatial basis functions (including different bases for different patches on the surface, if needed). The dimension of the basis that we employ is finite: $s = 1, 2, \dots, S$. The specific choice of S is discussed in Section 5.1. It is important, however, that the accuracy of representing the data at the boundary via the basis $\{\psi_s\}$ always be at least the same or better than the expected final accuracy of the numerical solution on the grid.

Consider the basis vector-functions $\boldsymbol{\psi}_{0,s} = (\psi_s, 0)$ and $\boldsymbol{\psi}_{1,s} = (0, \psi_s)$ that are used for building the expansions (27). Apply the equation-based extension operator (46) to each of these functions and subsequently compute $\boldsymbol{P}_{\gamma_{T_0}}$ and $\boldsymbol{R}_{\gamma_{T_0}}$ according to (41) and (43), respectively. Then, for each $s = 1, 2, \dots, S$ we obtain two pairs of vectors of dimension $|\gamma_{T_0}|$: $\boldsymbol{P}_{\gamma_{T_0}}\boldsymbol{Ex}\boldsymbol{\psi}_{0,s}$ and $\boldsymbol{R}_{\gamma_{T_0}}\boldsymbol{Ex}\boldsymbol{\psi}_{0,s}$ that correspond to $\boldsymbol{\psi}_{0,s}$ and $\boldsymbol{P}_{\gamma_{T_0}}\boldsymbol{Ex}\boldsymbol{\psi}_{1,s}$, and $\boldsymbol{R}_{\gamma_{T_0}}\boldsymbol{Ex}\boldsymbol{\psi}_{1,s}$ that correspond to $\boldsymbol{\psi}_{1,s}$, where $|\gamma_{T_0}|$ is the number of nodes in the grid boundary γ_{T_0}. The computation of these vectors for either $\boldsymbol{\psi}_{0,s} = (\psi_s, 0)$ or $\boldsymbol{\psi}_{1,s} = (0, \psi_s)$ requires one solution of the difference AP, i.e., $2S$ such solutions altogether.

Compose the matrices of the columns we have just introduced:

$$\begin{aligned}
\boldsymbol{Q}^{(0)}_{\gamma_{T_0}} &= \Big[\underbrace{\boldsymbol{P}_{\gamma_{T_0}}\boldsymbol{Ex}\boldsymbol{\psi}_{0,1} - \boldsymbol{Ex}\boldsymbol{\psi}_{0,1}}_{\text{column \# 1}} \dots \underbrace{\boldsymbol{P}_{\gamma_{T_0}}\boldsymbol{Ex}\boldsymbol{\psi}_{0,s} - \boldsymbol{Ex}\boldsymbol{\psi}_{0,s}}_{\text{column \# } s} \dots \underbrace{\boldsymbol{P}_{\gamma_{T_0}}\boldsymbol{Ex}\boldsymbol{\psi}_{0,S} - \boldsymbol{Ex}\boldsymbol{\psi}_{0,S}}_{\text{column \# } S}\Big], \\
\boldsymbol{Q}^{(1)}_{\gamma_{T_0}} &= \Big[\boldsymbol{P}_{\gamma_{T_0}}\boldsymbol{Ex}\boldsymbol{\psi}_{1,1} - \boldsymbol{Ex}\boldsymbol{\psi}_{1,1} \dots \boldsymbol{P}_{\gamma_{T_0}}\boldsymbol{Ex}\boldsymbol{\psi}_{1,s} - \boldsymbol{Ex}\boldsymbol{\psi}_{1,s} \dots \boldsymbol{P}_{\gamma_{T_0}}\boldsymbol{Ex}\boldsymbol{\psi}_{1,S} - \boldsymbol{Ex}\boldsymbol{\psi}_{1,S}\Big],
\end{aligned} \tag{47}$$

and

$$\begin{aligned}
\boldsymbol{R}^{(0)}_{\gamma_{T_0}} &= \Big[\underbrace{\boldsymbol{R}_{\gamma_{T_0}}\boldsymbol{Ex}\boldsymbol{\psi}_{0,1}}_{\text{column \# 1}} \dots \underbrace{\boldsymbol{R}_{\gamma_{T_0}}\boldsymbol{Ex}\boldsymbol{\psi}_{0,s}}_{\text{column \# } s} \dots \underbrace{\boldsymbol{R}_{\gamma_{T_0}}\boldsymbol{Ex}\boldsymbol{\psi}_{0,S}}_{\text{column \# } S}\Big], \\
\boldsymbol{R}^{(1)}_{\gamma_{T_0}} &= \Big[\boldsymbol{R}_{\gamma_{T_0}}\boldsymbol{Ex}\boldsymbol{\psi}_{1,1} \dots \boldsymbol{R}_{\gamma_{T_0}}\boldsymbol{Ex}\boldsymbol{\psi}_{1,s} \dots \boldsymbol{R}_{\gamma_{T_0}}\boldsymbol{Ex}\boldsymbol{\psi}_{1,S}\Big].
\end{aligned} \tag{48}$$

The horizontal dimension of each of these matrices is S and the vertical dimension is $|\gamma_{T_0}|$. The columns of the matrices $\boldsymbol{Q}^{(0)}_{\gamma_{T_0}}$ and $\boldsymbol{Q}^{(1)}_{\gamma_{T_0}}$ are the discrete counterparts of $\boldsymbol{Q}_{\Gamma_{T_0}}\boldsymbol{\psi}_{0,s}$ and $\boldsymbol{Q}_{\Gamma_{T_0}}\boldsymbol{\psi}_{1,s}$, respectively, from equation (28). Similarly, the columns of the matrices $\boldsymbol{R}^{(0)}_{\gamma_{T_0}}$ and $\boldsymbol{R}^{(1)}_{\gamma_{T_0}}$ are the discrete counterparts of $\boldsymbol{R}_{\Gamma_{T_0}}\boldsymbol{\psi}_{0,s}$ and $\boldsymbol{R}_{\Gamma_{T_0}}\boldsymbol{\psi}_{1,s}$, respectively, see (28). Arrange the coefficients $c^{(\mathrm{I})}_{0,s}$ and $c^{(\mathrm{I})}_{1,s}$, as well as $c^{(\mathrm{II})}_{0,s}$ and $c^{(\mathrm{II})}_{1,s}$, see Section 2.4, into vectors of dimension S:

$$\begin{aligned}
\boldsymbol{c}^{(\mathrm{I})}_0 &= \Big[c^{(\mathrm{I})}_{0,1} \dots c^{(\mathrm{I})}_{0,s} \dots c^{(\mathrm{I})}_{0,S}\Big]^T, \\
\boldsymbol{c}^{(\mathrm{I})}_1 &= \Big[c^{(\mathrm{I})}_{1,1} \dots c^{(\mathrm{I})}_{1,s} \dots c^{(\mathrm{I})}_{1,S}\Big]^T,
\end{aligned}$$

[9] There is no time variable in elliptic equations, so the expressions are modified accordingly.

$$\boldsymbol{c}_0^{(\mathrm{II})} = \left[c_{0,1}^{(\mathrm{II})} \dots c_{0,s}^{(\mathrm{II})} \dots c_{0,S}^{(\mathrm{II})}\right]^T,$$
$$\boldsymbol{c}_1^{(\mathrm{II})} = \left[c_{1,1}^{(\mathrm{II})} \dots c_{1,s}^{(\mathrm{II})} \dots c_{1,S}^{(\mathrm{II})}\right]^T.$$

Then, the fully discrete counterpart of equation (28) can be written as

$$\boldsymbol{Q}_{\gamma_{T_0}}^{(0)} \boldsymbol{c}_0^{(\mathrm{II})} + \boldsymbol{Q}_{\gamma_{T_0}}^{(1)} \boldsymbol{c}_1^{(\mathrm{II})} = -\boldsymbol{R}_{\gamma_{T_0}}^{(0)} \boldsymbol{c}_0^{(\mathrm{I})} - \boldsymbol{R}_{\gamma_{T_0}}^{(1)} \boldsymbol{c}_1^{(\mathrm{I})}. \tag{49}$$

The unknowns in equation (49) are the coefficients $\boldsymbol{c}_0^{(\mathrm{II})}$ and $\boldsymbol{c}_1^{(\mathrm{II})}$. They pertain to the continuous formulation in the sense that they are the coefficients of the expansion of the trace of a continuous solution at the continuous boundary. At the same time, the boundary equation with projection in (49) is enforced on the discretization grid, specifically, at the grid boundary γ_{T_0}. Similarly to (28), the coefficients $\boldsymbol{c}_0^{(\mathrm{I})}$ and $\boldsymbol{c}_1^{(\mathrm{I})}$ on the right-hand side of (49) are considered known. They represent the trace of the solution at the previous partition element, i.e., previous stage of time marching.

Equation (49) is supplemented by equation (29) that accounts for the boundary conditions. This is very convenient, as the latter is inherited straight from the original IBVP and thus formulated at the continuous boundary with respect to the same unknowns. The two equations together, (49) and (29), form a system to be solved for the coefficients $\boldsymbol{c}_0^{(\mathrm{II})}$ and $\boldsymbol{c}_1^{(\mathrm{II})}$. In doing so, equation (49) enforces the discrete BEP built on a subset of the regular (Cartesian) discretization grid. The continuous boundary does not have to conform to this grid and no approximation of the boundary conditions on the grid is required, because the boundary condition (29) is implemented directly.

4.7. Algorithm

Equations (49) and (29) describe a fully discrete version of the time-marching algorithm of Section 2.4. The simulation starts with precomputing the matrices $\boldsymbol{Q}_{\gamma_{T_0}}^{(0)}$, $\boldsymbol{Q}_{\gamma_{T_0}}^{(1)}$ and $\boldsymbol{R}_{\gamma_{T_0}}^{(0)}$, $\boldsymbol{R}_{\gamma_{T_0}}^{(1)}$ that all have the dimension of $S \times |\gamma_{T_0}|$. This requires a total of $2S$ solutions of the discretized AP (38), see Section 4.2.

The time marching is initiated by solving the discretized system (15), (16) for $T = T_0$:

$$\boldsymbol{Q}_{\gamma_{T_0}}^{(0)} \boldsymbol{c}_0^{(\mathrm{II})} + \boldsymbol{Q}_{\gamma_{T_0}}^{(1)} \boldsymbol{c}_1^{(\mathrm{II})} = -\boldsymbol{T}\boldsymbol{r}_{\gamma_{T_0}}^{(h)} \boldsymbol{G}^{(h)}\left(0, u_0^{(h)}, u_1^{(h)}\right), \tag{50}$$
$$\boldsymbol{I}_{\Gamma_{T_0}} \sum_s c_{0,s}^{(\mathrm{II})} \boldsymbol{\psi}_{0,s} + c_{1,s}^{(\mathrm{II})} \boldsymbol{\psi}_{1,s} = \phi_{T_0}. \tag{51}$$

Equation (50) is obtained directly from the inhomogeneous BEP (42′), where $u_0^{(h)}$ and $u_1^{(h)}$ are assumed to approximate the original initial conditions (2b) with second order accuracy on the first two time levels of the discretization grid. Equation (51) is the specification of the boundary condition (29) to the very first partition element that corresponds to $K = 1 \;\Leftrightarrow\; t \in (0, T_0]$.

Next, we make one time step by reassigning the coefficients: $\boldsymbol{c}_0^{(\mathrm{I})} \leftarrow\!\shortmid \boldsymbol{c}_0^{(\mathrm{II})}$ and $\boldsymbol{c}_1^{(\mathrm{I})} \leftarrow\!\shortmid \boldsymbol{c}_1^{(\mathrm{II})}$ and solving equations (49), (29) with respect to the new $\boldsymbol{c}_0^{(\mathrm{II})}$ and $\boldsymbol{c}_1^{(\mathrm{II})}$. All subsequent time steps are performed the same way. The coefficients are updated recursively as shown in Fig. 3. The time marching is conducted solely at the boundary, because both the data $\boldsymbol{c}_0^{(\mathrm{I})}$, $\boldsymbol{c}_1^{(\mathrm{I})}$ and the unknowns $\boldsymbol{c}_0^{(\mathrm{II})}$, $\boldsymbol{c}_1^{(\mathrm{II})}$ for each update pertain to the expansion of the solution with respect to the chosen basis at the continuous boundary of the domain where the solution is defined. If, at some point in time, the solution needs to be obtained inside Ω rather than only at $\partial\Omega$, it can be computed in the form of a difference potential $\boldsymbol{P}_{\mathbb{N}_{T_0}^+} \xi_{\gamma_{T_0}}$, where $\xi_{\gamma_{T_0}} = \boldsymbol{E}\boldsymbol{x}\boldsymbol{\xi}_{\Gamma_{T_0}}$ corresponds to the current partition element.

The system of equations (50), (51) is solved in the sense of least squares by QR factorization. The same solution methodology is used for system (49), (29). Least squares are chosen because $|\gamma_{T_0}|$ is typically larger than S so that both systems are formally overdetermined. As long as the original IBVP (2) has a unique (sufficiently smooth) solution, one may expect that the least squares minimum for systems (50), (51) and (49), (29) will be reached at zero (within the approximation accuracy on the grid).

The matrices on the left-hand side of equation (49) are the same as those on the left-hand side of equation (50) — they do not depend on time, i.e., on the partition index K. This is the same phenomenon as the time invariance of $\boldsymbol{Q}_{\Gamma_{T_0}} \boldsymbol{\psi}_{0,s}$ and $\boldsymbol{Q}_{\Gamma_{T_0}} \boldsymbol{\psi}_{1,s}$ in the semi-discrete setting of Section 2.4. If, in addition, the operator of the boundary conditions $\boldsymbol{I}_\Gamma$ appears time-independent so that $\boldsymbol{I}_{\Gamma_K}$ on the left-hand side of (29) does not depend on K (the data ϕ may still depend on t), then the QR decomposition needs to be performed only once ahead of time. It therefore becomes a part of the precomputing stage of the algorithm, and only backward substitution is done at every time step, i.e., at every transition from one partition element to the next. Numerical simulations of Section 5 are conducted for this case. Specific considerations related to computational complexity are discussed in Sections 5.3 and 5.4. They include, in particular, the analysis and demonstration of the efficiency of parallel implementation of the proposed algorithm (Section 5.4).

Finally, it is important to emphasize that since the boundary conditions are enforced by means of a separate equation (equation (51) or (29)), then the same set of operators $\boldsymbol{Q}_{\gamma_{T_0}}^{(0)}$, $\boldsymbol{Q}_{\gamma_{T_0}}^{(1)}$, $\boldsymbol{R}_{\gamma_{T_0}}^{(0)}$, and $\boldsymbol{R}_{\gamma_{T_0}}^{(1)}$ will allow one to handle various similar

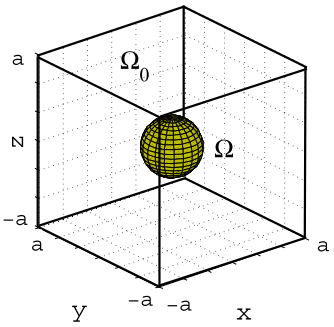

Fig. 7. Computational domain Ω and auxiliary domain Ω_0.

IBVPs (same geometry but different boundary conditions) at a very small additional computational cost. In particular, in Section 5.2 the operators were reused (rather than recomputed) for solving Dirichlet, Neumann, and Robin IBVPs.

5. Numerical experiments

5.1. Computational setup

Computational domains and grids The computational domain Ω is a ball of radius $R = 1$ centered at the origin of the Cartesian system, see Fig. 7. We solve the IBVP (2) on Ω, where the boundary condition (2c) may be of Dirichlet, Neumann, or Robin type. The specific Robin boundary condition that we use has the form:

$$\left(u + \frac{\partial u}{\partial \boldsymbol{n}}\right)\Big|_{\partial\Omega} = \phi. \tag{52}$$

Boundary condition (52) can be thought of as an "intermediate" case between the pure Dirichlet and pure Neumann boundary conditions.

The computational domain Ω is embedded into the auxiliary domain Ω_0 shaped as a cube: $\Omega_0 = [-a, a]^3$, see Fig. 7. The AP (38) is discretized and solved on Ω_0. In doing so, it is truncated with the homogeneous boundary conditions at $\partial\Omega_0$. The size a of the auxiliary cube Ω_0 is chosen sufficiently large so as to prevent the waves reflected from the outer boundary $\partial\Omega_0$ from reaching Ω over the time interval $2T_0$, as explained in Section 4.2. Specifically, $a = cT_0 + R$. As such, A depends on the size T_0 of a partition element (introduced in Section 2.2). In theory, T_0 can be as small as $\operatorname{diam}\Omega/c$. In practice, however, one needs to use a somewhat larger value: $T_0 \gtrsim \operatorname{diam}\Omega/c$, because the Huygens' principle holds in the discrete framework only approximately, rather than exactly. In other words, the backward dependence of the discrete solution in time stretches slightly beyond the predicted theoretical threshold. A detailed discussion of the discrete implementation of the algorithms based on the Huygens' principle can be found in [30,31]. In this paper, we merely take the value of T_0 as $T_0 = 2\operatorname{diam}\Omega/c$, which offers a very substantial "safety margin" and thus guarantees a proper behavior of the method.

An alternative to choosing the auxiliary domain Ω_0 sufficiently large so that the waves reflected off $\partial\Omega_0$ inwards won't reach Ω during the time interval $2T_0$ is to take a smaller Ω_0 but truncate it with a PML at $\partial\Omega_0$. This approach potentially makes solving the AP less expensive. The corresponding numerical simulations are presented in Section 5.4.

The domain Ω_0 is discretized with a sequence of Cartesian grids that we refer to as Grid 1, Grid 2, and Grid 3 (also Grid 4 in Section 5.3). The size of the coarsest grid (Grid 1) is $h = 2R/15$ so that there are 16 points per the diameter of the computational domain Ω. The overall Grid 1 on Ω_0 has 76 nodes in each coordinate direction. The time step is taken as $\tau = h/3$ to make sure that the CFL stability condition also holds with a safety margin. The three subsequent grids, Grid 2, Grid 3, and Grid 4, are obtained from Grid 1 by refining the latter by a factor of 2, 4, and 8, respectively. In all the computations of Section 5.2, the simulation time is $T = 2000\operatorname{diam}\Omega/c$, which is equivalent to 2000 times the time required for the waves to travel across the domain Ω.

Basis functions and symmetries As the computational domain Ω is a ball, we use a finite number of spherical harmonics $Y_{lm}(\theta, \varphi)$, $l = 0, 1, \ldots, L_{\max}$, $m = -l, \ldots, l$, as basis functions in space (i.e., on the boundary $\partial\Omega$). The basis functions in time are Chebyshev polynomials $T_n(t)$, $t \in [0, T_0]$, $n = 0, 1, ..., N_{\max}$. Thus, the overall space–time basis functions ψ_s on $\Gamma_{T_0} = \partial\Omega \times (0, T_0]$ (see Sections 2.4 and 4.6) are the products: $\psi_s = T_n(t)Y_{lm}(\theta, \varphi)$, where $s = \{l, m, n\}$.

The spherical harmonics with opposite m satisfy:

$$Y_{l,-m}(\theta, \varphi) = (-1)^m Y^*_{lm}(\theta, \varphi),$$

where the asterisk * denotes complex conjugate. Let $\boldsymbol{\psi}_{0,s} = (\psi_s, 0) = \big(T_n(t)Y_{lm}(\theta, \varphi), 0\big)$, as defined in Section 4.6, and let also $\boldsymbol{\psi}_{0,s'} = (\psi_{s'}, 0) = \big(T_n(t)Y_{l,-m}(\theta, \varphi), 0\big)$. Then, it is easy to see that

$$\boldsymbol{P}_{\gamma_{T_0}}\boldsymbol{E}\boldsymbol{x}\boldsymbol{\psi}_{0,s'} = (-1)^m\left(\boldsymbol{P}_{\gamma_{T_0}}\boldsymbol{E}\boldsymbol{x}\boldsymbol{\psi}_{0,s}\right)^*, \tag{53}$$

because the operator $\square_c^{(h)}$ and the Chebyshev polynomials are real.[10] The same is true for $\boldsymbol{\psi}_{1,s} = (0, \psi_s) = \big(0, T_n(t)Y_{lm}(\theta,\varphi)\big)$ and $\boldsymbol{\psi}_{1,s'} = (0, \psi_{s'}) = \big(0, T_n(t)Y_{l,-m}(\theta,\varphi)\big)$. Therefore, even though the dimension of the finite basis is $S = (1+N_{\max})(1+L_{\max})^2$, the actual number of discrete APs that need to be solved to obtain either $\boldsymbol{Q}^{(0)}_{\gamma_{T_0}}$ or $\boldsymbol{Q}^{(1)}_{\gamma_{T_0}}$ of (47) is only $(1+N_{\max})(1+L_{\max})(2+L_{\max})/2$ (see Section 4.6). The remaining columns of the matrices $\boldsymbol{Q}^{(0)}_{\gamma_{T_0}}$ and $\boldsymbol{Q}^{(1)}_{\gamma_{T_0}}$ are obtained with the help of (53). The same applies to $\boldsymbol{R}^{(0)}_{\gamma_{T_0}}$ and $\boldsymbol{R}^{(1)}_{\gamma_{T_0}}$ of (48). For the numerical simulations of Sections 5.2 through 5.4, we choose $N_{\max} = 11$ and $L_{\max} = 9$. These dimensions enable a sufficiently accurate representation of the boundary data on $\Gamma_{T_0} = \partial\Omega \times (0, T_0]$, which allows us to demonstrate the convergence of the numerical solution on fine grids.

Reference solution The monochromatic plane wave

$$u_{\text{ref}}(\boldsymbol{x}, t) = \cos(\boldsymbol{k}\cdot\boldsymbol{x} - \omega t) \tag{54}$$

solves the three-dimensional homogeneous wave equation (2a) and is used as a reference solution with $\omega = 1$ and $\boldsymbol{k} = \frac{\omega}{\sqrt{3}}(1,1,1)$ so that the dispersion relation holds: $|\boldsymbol{k}| \equiv k = \omega/c$. The data for the initial and boundary conditions (2b) and (2c) are derived from (54) at $t = 0$ and on Γ, respectively.

Expanding $e^{i\boldsymbol{k}\cdot\boldsymbol{x}}$ over the spherical functions and $e^{-i\omega t}$ over the Chebyshev polynomials, one can represent the trace of the reference solution (54) on $\partial\Omega$ as follows:

$$\cos(\boldsymbol{k}\cdot\boldsymbol{x} - \omega t)|_{\partial\Omega} = \sum_{n=0}^{\infty}\sum_{l=0}^{\infty}\sum_{m=-l}^{l} A_{nlm}(\omega,\boldsymbol{k})Y_{lm}(\theta,\varphi)T_n\left(\frac{2t-T_0}{T_0}\right), \tag{55}$$

where the polar angle θ and azimuthal angle φ correspond to a given $\boldsymbol{x} \in \partial\Omega$. The argument of T_n ranges from -1 to 1 as the time t ranges between 0 and T_0. The coefficients $A_{nlm}(\omega,\boldsymbol{k})$ are given by:

$$A_{nlm}(\omega,\boldsymbol{k}) = 2\pi i^{n+l} j_l(kR)\left\{a_n(\omega) + (-1)^l a_n(-\omega)\right\} Y^*_{lm}(\theta',\varphi'), \tag{56}$$

where

$$a_n(\omega) = (-1)^n e^{-i\omega(t_0+T_0/2)} J_n(\omega T_0/2) \times \begin{cases} 1, & n = 0, \\ 2, & n > 0. \end{cases} \tag{57}$$

The angles θ' and φ' in (56) determine the direction of $\boldsymbol{k}$, and $j_l(\cdot)$ denotes the spherical Bessel function. In (57), $J_n(\cdot)$ is the Bessel function of the first kind.

Formulae (55)–(56) provide the coefficients $\boldsymbol{c}_0$ required for the solution of the Dirichlet problem. For the Neumann problem one needs $\boldsymbol{c}_1$, i.e., the expansion of the normal derivative of (54) on $\partial\Omega$, which can be obtained from (55)–(56) by differentiating with respect to R. The resulting expression is, again, given by (55) with the substitution $j_l(kR) \to k j_l'(kR)$ in (56), where $j_l'(\cdot)$ is the first derivative of the spherical Bessel function. The Robin boundary condition (52) yields a relationship between $\boldsymbol{c}_0$ and $\boldsymbol{c}_1$ rather than the actual values of the specific coefficients. So in this case no expressions similar to (56) are required. Instead, the aforementioned relations between $\boldsymbol{c}_0$ and $\boldsymbol{c}_1$ become a part of the overall linear system that is solved by least squares.

Conditioning Since system (50), (51), as well as system (49), (29), will be solved by least squares, it is useful to estimate the condition number of the corresponding system matrix. For simplicity, we choose the Dirichlet problem and consider the rectangular matrix $\boldsymbol{Q}^{(1)}_{\gamma_{T_0}}$, see formula (47). Its condition number in the sense of the Euclidean norm $\|\cdot\|_2$ is given by (see [43, pages 94-95]):

$$\kappa\big(\boldsymbol{Q}^{(1)}_{\gamma_{T_0}}\big) = \big\|\boldsymbol{Q}^{(1)}_{\gamma_{T_0}}\big\|_2 \big\|\boldsymbol{Q}^{(1)+}_{\gamma_{T_0}}\big\|_2 = \frac{\sigma_{\max}}{\sigma_{\min}},$$

where the superscript $+$ denotes the Moore–Penrose pseudo-inverse, and $\sigma_{\max}$ and $\sigma_{\min}$ are the largest and smallest singular values of $\boldsymbol{Q}^{(1)}_{\gamma_{T_0}}$, respectively. The singular values are computed numerically on four consecutive grids and the results are summarized in Table 1.

From Table 1, we see that the condition number of $\boldsymbol{Q}^{(1)}_{\gamma_{T_0}}$ decreases as the grid is refined. This behavior indicates that the problem we will be solving by least squares is well conditioned. If the grid were to be refined further (beyond Grid 4), we expect that the condition number would approach (asymptotically) a sufficiently small limit value. As far as the mechanism

[10] See Section 4.4 for the construction of difference potentials/projections, in particular, the operator $\boldsymbol{P}_{\gamma_{T_0}}$, and Section 4.5 for the construction of the equation-based extension $\boldsymbol{E}\boldsymbol{x}$.

Table 1
Maximum and minimum singular values and the condition number of $\boldsymbol{Q}^{(1)}_{\gamma_{T_0}}$.

	$\sigma_{\max}$	$\sigma_{\min}$	$\kappa\left(\boldsymbol{Q}^{(1)}_{\gamma_{T_0}}\right)$
Grid 1	14.94	5.15×10^{-3}	2901
Grid 2	40.44	6.51×10^{-2}	621
Grid 3	110.85	2.98×10^{-1}	372
Grid 4	306.65	1.07	287

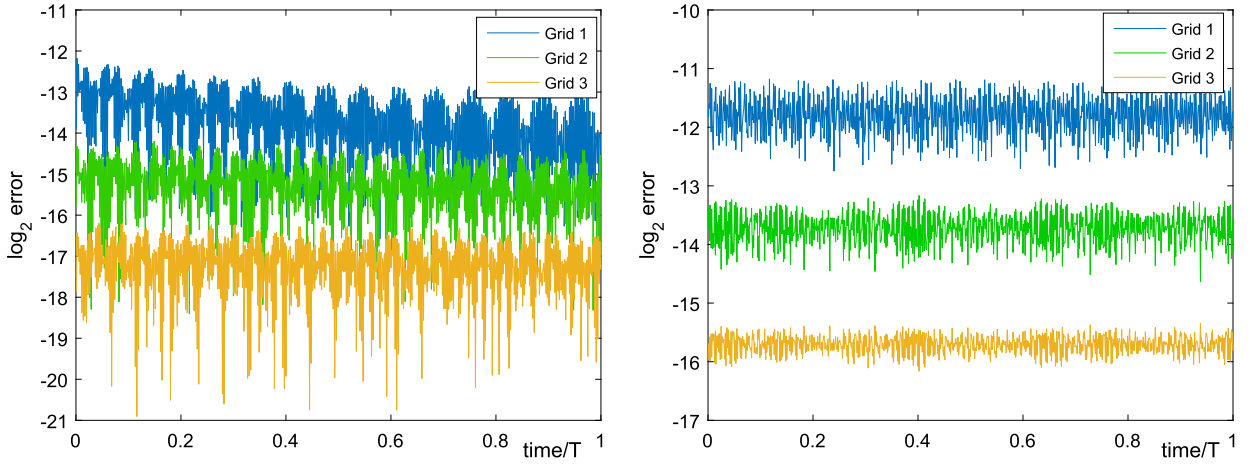

(a) Dirichlet boundary condition (b) Robin boundary condition

Fig. 8. Grid convergence in the maximum norm of the finite-difference solution on the domain Ω; the simulation time $T = 2000\ \mathrm{diam}\Omega/c$. Upper graph — Grid 1; middle graph — Grid 2; lower graph — Grid 3.

of improvement of the condition number shown in Table 1, we attribute it to the system of grid functions $\{\boldsymbol{Ex\psi}_{1,s}\}_{s=1}^{S}$ that help define $\boldsymbol{Q}^{(1)}_{\gamma_{T_0}}$ in (47) becoming closer to orthogonal on finer grids. Indeed, while the continuous basis functions $\boldsymbol{\psi}_{1,s}$ are chosen orthogonal, their extensions $\boldsymbol{Ex\psi}_{1,s}$ to the grid boundary γ_{T_0} do not, generally speaking, maintain this property. However, on finer grids the grid boundary γ_{T_0} straddles the continuous boundary Γ_{T_0} "tighter" and hence the grid functions $\boldsymbol{Ex\psi}_{1,s}$ move closer to orthogonal.

The condition number of the matrix $\boldsymbol{Q}^{(0)}_{\gamma_{T_0}}$ of (47) that is used for solving the Neumann problem behaves basically the same way as the condition number of $\boldsymbol{Q}^{(1)}_{\gamma_{T_0}}$ shown in Table 1.

5.2. Results of computations: grid convergence and accuracy analysis

In this section, we present the numerical results for the Dirichlet, Neumann, and Robin IBVPs. Since these problems share the same geometry, then on a given grid they are solved using the same operators $\boldsymbol{Q}^{(0)}_{\gamma_{T_0}}$, $\boldsymbol{Q}^{(1)}_{\gamma_{T_0}}$, $\boldsymbol{R}^{(0)}_{\gamma_{T_0}}$, and $\boldsymbol{R}^{(1)}_{\gamma_{T_0}}$. The operators do not need to be recomputed when the boundary condition changes.

In Figs. 8a and 8b we show the error profiles for the Dirichlet and Robin boundary conditions, respectively, as functions of the time t. These figures clearly demonstrate that there is no error accumulation over time, and that the numerical solution converges to the reference solution (54) uniformly in time with the design rate of the scheme (second order) as the grid is refined.

The performance of the method in the case of a Neumann boundary condition is, however, different. As indicated by Fig. 9a, the error accumulates linearly in time. The rate of accumulation decreases as the grid is refined, and at any fixed moment of time one still observes the design second order grid convergence. Yet the error grows as the time elapses.

However, the growth of the error is completely eliminated if, instead of the finite difference solution itself, we consider its gradient, i.e., the derivative in a given spatial direction. This is demonstrated in Fig. 9b that shows three temporally uniform error profiles for the gradient of the solution and thus corroborates the grid convergence with the design rate of the scheme.

In Table 2, we summarize the grid convergence results that correspond to Figs. 8a, 8b, and 9b. Convergence rates are calculated by taking a square root of the ratio of errors on two subsequent grids. In all cases, the method demonstrates the design second order convergence.

The phenomenon of error accumulation shown in Fig. 9a is specific to the Neumann boundary conditions. We have not observed any growth of the error in any simulations that we conducted with either Dirichlet or Robin boundary conditions.

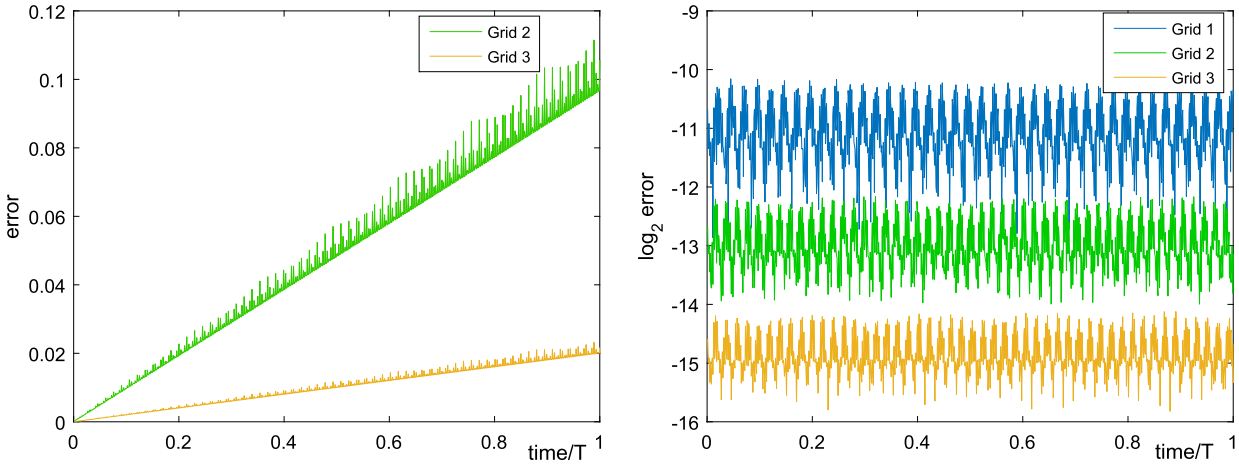

(a) The solution itself (b) Gradient of the solution

Fig. 9. Grid convergence in the maximum norm of the finite-difference solution on the domain Ω in the case of the Neumann boundary condition; the simulation time $T = 2000\,\mathrm{diam}\Omega/c$. Panel (a): upper graph — Grid 2; lower graph — Grid 3. Panel (b): upper graph — Grid 1; middle graph — grid 2; lower graph — Grid 3.

Table 2
Time averaged error on different grids and convergence rates calculated from plots 8a, 8b, and 9b.

	Grid 1	Grid 2	Rate	Grid 3	Rate
Dirichlet BC	8.03×10^{-5}	2.64×10^{-5}	1.74	6.87×10^{-6}	1.96
Robin BC	2.89×10^{-4}	7.50×10^{-5}	1.96	1.87×10^{-5}	1.99
Neumann BC (∇)	4.86×10^{-4}	1.29×10^{-4}	1.94	3.48×10^{-5}	1.92

We attribute this phenomenon to the fact that the linear function $a+bt$ satisfies both the homogeneous d'Alembert equation and homogeneous Neumann boundary condition. Therefore, small perturbations of the initial data may give rise to the spurious solution $a + bt$ that increases as the time elapses. This spurious mode does not exist for either Dirichlet or Robin boundary conditions. Taking a spatial gradient of the solution eliminates it in the Neumann casel. Hence, there is no error accumulation in Fig. 9b. A rigorous derivation of the formulae that yield solutions to IBVPs for the d'Alembert equation (including the Neumann case) can be found in [44, Chapter 2]; it is based on separation of variables.

In Appendix A, we discuss the phenomenon of error growth for Neumann IBVPs in more detail, and also present the results of additional numerical simulations. We emphasize that this phenomenon is apparently not related to our specific numerical method that is based on difference potentials and the Huygens' principle. Indeed, in Appendix A we observe the same behavior of the error in the case of straightforward integration of a Neumann IBVP for the wave equation on the Cartesian grid in a rectangular box.

A certain deterioration of numerical performance for Neumann boundary conditions has been previously reported in the literature, e.g., in the case of spectral methods [45].

Fortunately, in most physical applications, a Neumann IBVP for the wave equation would be formulated for the potential of the field rather than for the field itself (e.g., vector and scalar potentials in electrodynamics, velocity potential in fluid mechanics, etc.). To obtain the observable quantity, i.e., the field, one needs to differentiate the potential, which removes the error growth.

5.3. Computational complexity for a fixed time interval

In the next two sections, we analyze the complexity of the boundary time-marching algorithm of Section 4.7 and compare it against that of the conventional volumetric time marching. The volumetric integration is conducted by means of the same finite difference scheme as used for solving the discrete AP in Section 4.2, but applied to the original problem (2) on a simple domain, namely, the cube $[-R, R]^3$. Although the latter is somewhat larger than the ball $\Omega = \{r \leqslant R\}$, this choice involves no special treatment of curvilinear boundaries on the Cartesian grid and is sufficient for the purpose of comparison.

In Fig. 10, we plot the computational time $\mathrm{CPU}(T_0)$ required to advance the numerical solution over a fixed interval T_0 of physical time on the successive grids, Grid 1 through Grid 4. The interval T_0 is chosen as a natural time scale, see (23), and each subsequent grid is a refinement of the previous one by a factor of 2. In the case of a conventional volumetric time marching by means of an explicit scheme, the execution time $\mathrm{CPU}(T_0)$ is proportional to the overall number of grid nodes used by the algorithm during the time interval T_0:

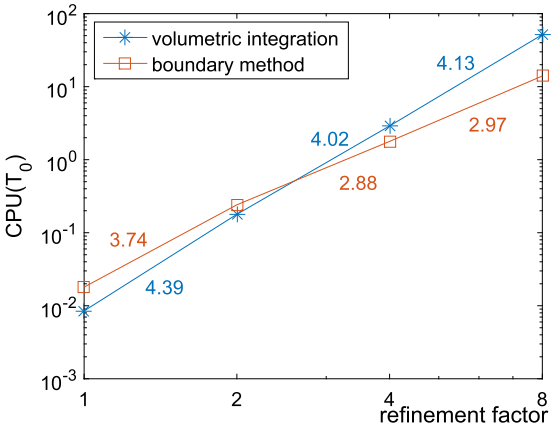

Fig. 10. Log–log plot of the computational time vs. grid dimension (i.e., the refinement factor relative to the coarsest grid — Grid 1) for computing the solution during the physical time interval T_0 on four successive grids.

$$\begin{aligned} &\mathrm{CPU}(T_0) = \mathrm{const} \times (\text{number of time steps per } T_0) \times N^3 = \mathrm{const} \times N^4, \\ &\qquad \text{or} \quad \ln \mathrm{CPU}(T_0) \propto 4 \ln N. \end{aligned} \tag{58}$$

In (58), N is the grid dimension in one spatial direction. In addition, we assume that $cT_0 \sim \mathrm{diam}\Omega = 2R$ and the time step is proportional to the spatial grid size so that the number of steps per T_0 will scale linearly with respect to N. This yields a total of $\mathcal{O}(N^4)$ grid nodes in space–time over the interval T_0. The computational cost directly proportional to N^4, see (58), indicates a linear computational complexity with respect to the grid dimension.

In the case of the boundary approach, we expect

$$\mathrm{CPU}(T_0) = \mathrm{const} \times S \times N^3, \quad \text{or} \quad \ln \mathrm{CPU}(T_0) \propto 3 \ln N. \tag{59}$$

Indeed, the linear system (50), (51) (or (49), (29)) is solved by least squares, i.e., by QR factorization. The horizontal dimension of this system is equal to the number of basis functions S, see formula (47), while its vertical dimension is $|\gamma_{T_0}| \sim N^3$. The cost of factorization itself, however, is not included into $\mathrm{CPU}(T_0)$ of (59); this quantity accounts only for the cost of backward substitution performed after the factors Q and R have been determined. The number of basis functions S is chosen ahead of time and fixed for the entire range of simulations on a sequence of grids, see Section 5.1. Hence, formula (59) shows a sub-linear complexity with respect to the grid dimension, because the computational cost in (59) grows slower than the total number of grid nodes. Note, however, that the cost of precomputing the operators in equation (49) is not included into the estimate (59) either. This cost, along with the cost of QR factorization per se, will be addressed in the context of parallelization, see Section 5.4.

Fig. 10 suggests that $\mathrm{CPU}(T_0)$ indeed behaves as predicted by formulae (58) and (59) when N increases 2, 4, and 8 times. To facilitate the comparison, we explicitly show the slopes of individual segments of the log–log lines (58) and (59) between the successive grid refinements. Fig. 10 also indicates that the boundary method outperforms the volumetric one only on sufficiently fine grids. The reason is that on coarse grids, the "thickness" of γ_{T_0} may be comparable to the size of the computational domain, see Figs. 5c and 6, so the boundary problem does not benefit yet from its reduced dimensionality. As the grid is refined, the dependence of the actual cost on N involves specific proportionality constants (fixed values determined by a given method) both in formula (58) and in formula (59). In the case of the boundary method, see (59), the cost is also proportional to the number of basis functions S (which is fixed as well). While it is clear that as N increases, the right-hand side of the first equation in (58) grows faster than that in (59) and will eventually dominate, the specific value of N where the two curves intersect depends on the aforementioned constants. As Fig. 10 shows, for our particular computational setting the intersection occurs somewhere between Grid 2 and Grid 3.

5.4. Computational complexity over long runs and parallelization in time

The operators $\boldsymbol{Q}^{(0)}_{\gamma_{T_0}}$, $\boldsymbol{Q}^{(1)}_{\gamma_{T_0}}$, $\boldsymbol{R}^{(0)}_{\gamma_{T_0}}$, and $\boldsymbol{R}^{(1)}_{\gamma_{T_0}}$ that appear in equation (49) need to be computed prior to starting the time marching. According to formulae (47) and (48), this requires solving the discrete AP on the interval $2T_0$ for each basis function $\boldsymbol{\psi}_{0,s}$ or $\boldsymbol{\psi}_{1,s}$, $s = 1, 2, \ldots, S$, which is a major contribution to the overall computational complexity. The overall number of APs M that need to be solved is reduced due to symmetry, see Section 5.1, but may still remain substantial. For our simulations, we take $N_{\max} = 11$ and $L_{\max} = 9$, which yields a total of $M = (1 + N_{\max})(1 + L_{\max})(2 + L_{\max})/2 = 660$ APs to integrate. However, this workload can be distributed over multiple computational cores with high efficiency, since different APs are completely independent from one another. Hence, ideally, the time needed to precompute the operators in equation (49) should decrease proportionally to the number of cores.

All the simulations reported in the current paper are performed on a 32-core Dell PowerEdge server with two Intel® Xeon® CPU E5-2698 v3 2.30GHz processors and 512 Gb RAM, running Linux OS. In our code, the APs are split into groups of 32 as per the number of cores. Numerical solution of each AP is rendered by a Fortran subroutine (Intel® Parallel Studio XE Composer Edition for Fortran) that takes a given basis function $\boldsymbol{\psi}_{0,s}$ or $\boldsymbol{\psi}_{1,s}$ as input. This subroutine with different input data is cloned for parallel execution on 32 computational cores using OpenMP 3.0 API. For a shared memory architecture, this appears a relatively easy task. On the coarsest grid (Grid 1), the single-core and multi-core runs take 70.28 and 3.32 seconds, respectively, which yields a speed-up of approximately 21 times or, equivalently, the parallelization efficiency of about 66%. On the next grid (Grid 2), the computational times are 1128.61 and 54.26 seconds, respectively, which again, yields the same acceleration by approximately a factor of 21. On finer grids, the acceleration factor remains around 20. This is still less than the theoretical limit of 32, which would correspond to a 100% parallelization efficiency in distributing the independent APs between the computational cores. The reason for having a somewhat reduced parallelization efficiency may be related to hardware (shared memory as opposed to distributed memory) or software or both. In this paper though, we do not pursue a further increase of parallelization efficiency and rather leave this objective for the future.

The overall computational complexity of the algorithm as a function of the physical time t, measured in terms of the execution time: $\mathrm{CPU} = \mathrm{CPU}(t)$, behaves differently for the conventional volumetric time marching and boundary time marching. In the case of a conventional marching, the execution time is directly proportional to the physical time:

$$\mathrm{CPU}_{\mathrm{vol}}(t) = C_{\mathrm{vol}} t, \tag{60}$$

where C_{vol} is a constant that depends on the grid dimension.[11] The value of C_{vol} can be easily determined from the data presented in Fig. 10. On a given grid, one merely has $C_{\mathrm{vol}} = \mathrm{CPU}(T_0)/T_0$, where $\mathrm{CPU}(T_0)$ is introduced in equation (58).

For the boundary time marching, the complexity is given by

$$\mathrm{CPU}_{\mathrm{bnd}}(t) = \mathrm{CPU}_0 + C_{\mathrm{bnd}} t. \tag{61}$$

In formula (61), CPU_0 is the initiation cost needed for precomputing the operators $\boldsymbol{Q}^{(0)}_{\gamma_{T_0}}$, $\boldsymbol{Q}^{(1)}_{\gamma_{T_0}}$, $\boldsymbol{R}^{(0)}_{\gamma_{T_0}}$, and $\boldsymbol{R}^{(1)}_{\gamma_{T_0}}$, as well as performing the QR factorization for the resulting linear system (49), (29), while C_{bnd} is another constant that depends on the grid dimension. Similarly to C_{vol} of (60), the value of C_{bnd} in (61) can be obtained from the data presented in Fig. 10: $C_{\mathrm{bnd}} = \mathrm{CPU}(T_0)/T_0$, where $\mathrm{CPU}(T_0)$ is introduced in equation (59) (it does not include the initiation cost).

The sub-linear complexity of the boundary method implies that on sufficiently fine grids we have $C_{\mathrm{bnd}} < C_{\mathrm{vol}}$, and the finer the grid the more significant is the difference. This is evident from Fig. 10, see also formulae (58) and (59). Therefore, even though CPU_0 presents a substantial contribution to the overall complexity of the boundary method, see (61), the slower rate of increase in (61) compared to (60) implies that there exist a break-even simulation time t_{BE} beyond which the boundary time marching outperforms the volumetric one. The behavior of $\mathrm{CPU}_{\mathrm{vol}}(t)$ and $\mathrm{CPU}_{\mathrm{bnd}}(t)$, including the determination of t_{BE}, is schematically shown in Fig. 11, while from (60) and (61), we find:

$$t_{\mathrm{BE}} = \frac{\mathrm{CPU}_0}{C_{\mathrm{vol}} - C_{\mathrm{bnd}}}. \tag{62}$$

According to (62), the value of t_{BE} depends on CPU_0; the larger the initiation cost, the further away on the horizontal axis the moment t_{BE} is located, see Fig. 11. The initiation cost CPU_0, in its own right, is the cost of solving a predetermined number M of APs on the time interval $2T_0$ (proportional to $M \times N^4$) plus the one-time cost of QR factorization (proportional to $S^2 \times N^3$). Beyond the initial execution time CPU_0, the specific cost of the boundary method, i.e., its cost per unit time, becomes (much) lower than that of the volumetric method, and the lower the finer the grid. Therefore, at $t = t_{\mathrm{BE}}$ the overall cost of the boundary method also becomes lower than that of the volumetric method.

Moreover, as we have shown, the computation of the operators in equation (49) can be efficiently parallelized on a multi-processor (or multi-core) platform. The same is true regarding the QR factorization. It can be computed very efficiently by the standard Mathematics Kernel Library (MKL), which is a part of Intel® Parallel Studio. In doing so, the cost of computing the QR factorization appears negligible compared to the cost of solving M APs over the time interval $2T_0$. Therefore, from now on we will be assuming that the initiation cost CPU_0 consists of only solving the APs. In the case of a sequential implementation, this cost is obviously the same as what would have been the cost of integrating a single AP over a long time interval — the interval equal to $2T_0M$, where M is the number of APs. In the case of a parallel implementation, the actual wall-clock time for this computation becomes

$$\mathrm{CPU}'_0 = \frac{\mathrm{CPU}_0}{P}, \tag{63}$$

where P is the factor that determines the parallelization efficiency. In our simulations, the value of P varied between 20 and 21, with the theoretical limit of 32 on a 32-core system. Given the relation (63), one can interpret the execution time

[11] Recall, the volumetric integration that we need for comparison purposes is performed on a cube $[-R, R]^3$, where R is the radius of the ball Ω, see the beginning of Section 5.3.

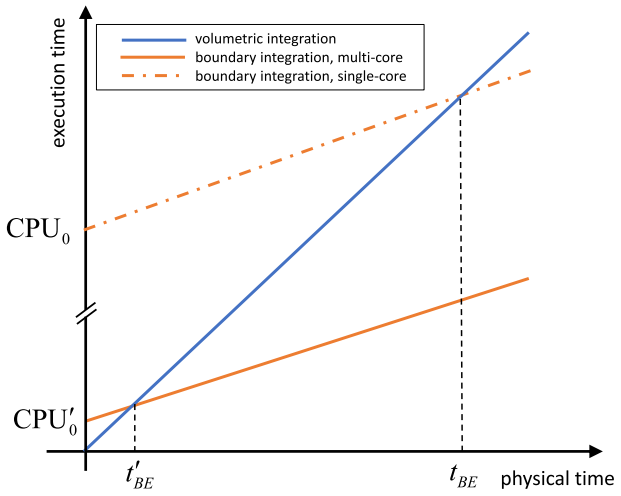

Fig. 11. Schematic dependence of the execution time CPU(t), i.e., the computational cost, on the physical time t for the volumetric and boundary time marching. The actual data are summarized in Table 3.

Table 3
Parameters of the simulation that characterize the complexity.

	C_{bnd}, sec/T_0	C_{vol}, sec/T_0	CPU$'_0$, sec	t'_{BE}, T_0
Grid 3	1.8	2.3	766	1532
Grid 4	15	49	12792	376

CPU$'_0$ as the cost of integrating a single AP over the time interval $2T_0M/P$, which is P times shorter than the interval $2T_0M$ that corresponds to a fully sequential, i.e., single-core, implementation. This can be thought of as parallelization in time.

Accordingly, in Fig. 11 we schematically show two graphs of complexity for the boundary method. The first one corresponds to equation (61) with the full non-modified initiation cost CPU$_0$, and the second one corresponds to the modified equation:

$$\text{CPU}'_{\text{bnd}}(t) = \text{CPU}'_0 + C_{\text{bnd}}t, \tag{61′}$$

with the new initiation cost CPU$'_0$ that is reduced by a factor of P due to parallelization. We are also showing two break-even moments of time, one given by (62) and the other one that corresponds to parallelization in time:

$$t'_{\text{BE}} = \frac{\text{CPU}'_0}{C_{\text{vol}} - C_{\text{bnd}}} = \frac{t_{\text{BE}}}{P}. \tag{62′}$$

Formula (62′) is obtained from (61′) and (60).

The AP can be solved on a large domain Ω_0 that won't allow the reflections from its outer boundary to reach the interior domain Ω during the time interval $2T_0$, see Fig. 7, or it can be solved on a smaller domain Ω_0 terminated with a PML. The second approach is potentially less expensive. Hence, in our subsequent simulations we employ a Cartesian PML for the 3D wave equation proposed in [46]. We also note that a comparative study of complexity for the various treatments of the artificial outer boundary is available in [47]. As our test solution (54) has a fairly long wavelength: $2\pi/|\boldsymbol{k}| = 2\pi$, we could not make the PML too narrow and took its width as approximately 0.67, where the diameter of the computational domain Ω is equal to 2. The damping profile of the PML was chosen quadratic, with the damping constant $\zeta_i = 75$ in each spatial dimension. Overall, the use of the PML [46] has allowed us to reduce the grid dimension on the auxiliary domain Ω_0 from $76 \times 76 \times 76$ to $45 \times 45 \times 45$ for our coarsest grid — Grid 1. For the finer grids, the relative reduction of dimension was the same.

In Table 3, we present the values of C_{bnd}, C_{vol}, CPU$'_0$, and t'_{BE} (measured in the units T_0) on Grid 3 and Grid 4 in the case of the AP terminated with a PML. The quantities C_{bnd} and C_{vol} are obtained from the data presented in Fig. 10, as suggested previously.[12]

As Table 3 indicates, the value of CPU$'_0$ increases by roughly a factor of 16 when the grid is refined by factor of 2 (this follows the $\mathcal{O}(N^4)$ asymptotic that characterizes the plain volumetric integration employed at the precomputing stage). The value of C_{vol} has increased by a factor of 21 between Grid 3 and Grid 4 (theoretically, it was supposed to be a factor of

[12] More accurate estimates of C_{bnd} and C_{vol} on the time interval of length $100T_0$ yield the same results.

16), while the value of C_{bnd} has increased by a factor of 8, as predicted by analysis. As a result, the break-even time t'_{BE} has dropped by a factor of 4.

The scaling shown in the first three columns of Table 3 is expected to remain the same if the grid were to be further refined. Namely, every reduction of the grid size by a factor of 2 should cause the increase of CPU'_0 and C_{vol} by a factor of 16, and the increase of C_{bnd} by a factor of 8. After n successive refinements starting from a given grid, we obtain with the help of formula (62′):

$$t'^{(n)}_{\text{BE}} = \frac{\text{CPU}'_0}{C_{\text{vol}} - \frac{C_{\text{bnd}}}{2^{n-1}}}. \tag{64}$$

Expression (64) shows that on one hand, on finer grids the break-even time is shorter, which makes the boundary method more beneficial. On the other hand, the relative cost of the boundary time marching compared to that of the conventional volumetric time marching becomes progressively smaller (compare the two terms in the denominator on the right-hand side of (64)). Asymptotically on very fine grids (as we formally take $n \to \infty$ in (64)), this cost can be disregarded. Then, the break-even time approaches a finite limit: $t'^{(n)}_{\text{BE}} \to \text{CPU}'_0/C_{\text{vol}}$. In other words, on sufficiently fine grids one can think that the cost of the boundary method beyond the initiation expense is negligible.

It is to be reiterated that the initiation cost CPU'_0 that has already been reduced by parallelization, can also be shared between multiple similar problems (e.g., problems with the same geometry but different boundary conditions). This further increases the overall efficiency of the proposed boundary method. For example, all the solutions presented in Section 5.2 (Dirichlet, Neumann, and Robin boundary conditions) were computed using one and the same set of operators $\boldsymbol{Q}^{(0)}_{\gamma_{T_0}}$, $\boldsymbol{Q}^{(1)}_{\gamma_{T_0}}$, $\boldsymbol{R}^{(0)}_{\gamma_{T_0}}$, and $\boldsymbol{R}^{(1)}_{\gamma_{T_0}}$ on a given grid. We needed to recompute the operators only on a new (finer) grid, while on the same grid they were reused, and the initiation cost CPU'_0 was incurred only once.

6. Discussion

By combining the method of difference potentials with the Huygens' principle, we have built a boundary time marching algorithm for the unsteady wave equation that offers a better computational complexity (sub-linear) that of the conventional volumetric time marching. The performance of the proposed algorithm has been demonstrated experimentally by solving a range of interior IBVPs with the Dirichlet, Neumann, and Robin boundary conditions.

Our algorithm uses only regular structured grids yet allows one to discretize the formulations that involves general non-conforming geometries with no loss of accuracy. It also facilities sharing the computational cost between multiple similar problems. On multi-processor (multi-core) systems the algorithm takes advantage of what can be thought of as parallelization in time.

The possible future extensions include going from second order accuracy to high order accuracy (which is important for the numerical simulation of waves as it reduces the dispersion error), running the computations for exterior problems, addressing more realistic geometries, getting better parallelization efficiency, and moving from scalar governing equations to systems (e.g., Maxwell's).

High order accuracy can be achieved by replacing the currently used central difference second order accurate scheme with a compact high order accurate scheme [35]. In doing so, the grid sets defined in Section 4.3 may change and the extension operators of Section 4.5 may need to be built to higher order, but the rest of the algorithm will stay unaffected.

The simulation of exterior problems is expected to be even more beneficial from the standpoint of complexity than the simulation of interior problems. The reason is that the proposed boundary method requires solving the AP that involves a PML, which increases the overall grid dimension and adds the cost (per unit time) compared to the plain interior problem. In the case of exterior problems, however, the reference volumetric time marching will also have to include a PML, which will place both methods on an equal footing and make the break-even time much shorter.

Let us also note that as the Huygens' principle allows one to solve the AP only on a finite time interval, then for the boundary time marching it eliminates any potential concerns related to the long-time performance of the chosen PML. In [48,30,31,49], we have employed lacunae and the Huygens' principle for the stabilization of ABCs and PMLs over long simulation times.

Extension to systems will begin with obtaining the vector counterparts to the Green's formulae (5) and (31). The parallelization efficiency may be improved by porting the code to a different hardware architecture and/or making the appropriate software modifications.

Appendix A. Numerical solution of the wave equation subject to Neumann boundary conditions

Our goal here is to demonstrate that the linear growth of the error that we observed in Section 5.2 in the case of a Neumann boundary condition, see Fig. 9a, is not related to the application of the MDP and/or the Huygens' principle, and can rather be reproduced for the simplest "textbook" discretization as well.

To that end, consider an interior Neumann IBVP (2) for the three-dimensional wave equation on the domain of a simple shape — a cube $\Omega = [-R_0, R_0]^3$. We will solve this problem numerically using the same second order accurate central

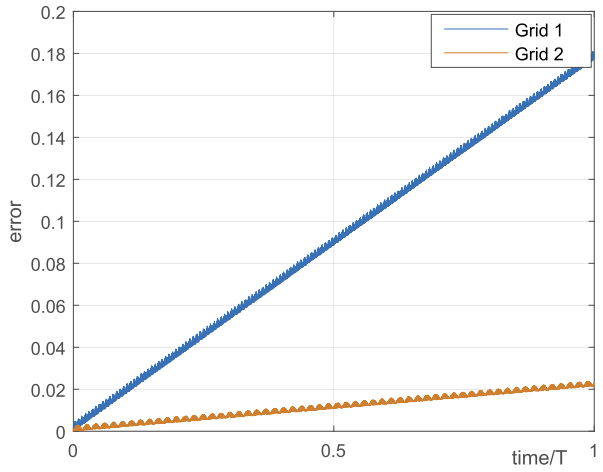

(a) Solution of the Neumann problem

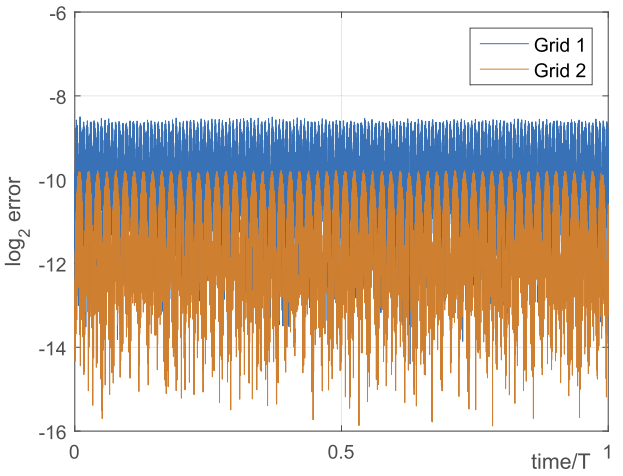

(b) Gradient of the solution

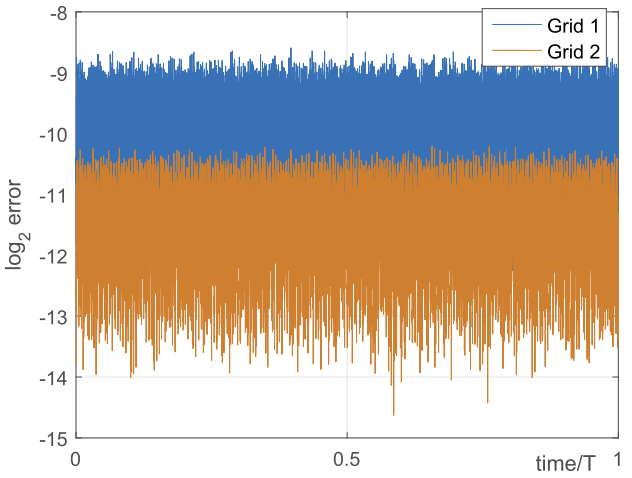

(c) Solution of the mixed problem

Fig. 12. Error profiles in the maximum norm for the Neumann and mixed problem solved on a Cartesian cube. A log-linear scale is used in the panels (b) and (c). Upper graph — Grid 1; lower graph — Grid 2.

difference scheme as used for solving the AP, see Section 4.2. To approximate the Neumann boundary conditions with second order accuracy, we choose the uniform Cartesian grid in such a way that the boundary of the cube Ω would cross through its cell centers rather than actual nodes. Then, the normal derivative can be approximated with second order accuracy as follows:

$$\left.\frac{\partial u}{\partial \boldsymbol{n}}\right|_{i+1/2} \approx \frac{u_{i+1} - u_i}{h},$$

where the subscript i corresponds to the direction of differentiation. For the numerical demonstrations in this section, we will use the same plane wave test solution (54) as used in Section 5.2.

In Fig. 12, we plot the maximum norm of the error as a function of time. Fig. 12a corresponds to the error of the Neumann solution itself, and one can clearly see that this error increases linearly as the time elapses (cf. Fig. 9a). In contrast to that, the gradient of the solution shows no error accumulation at all for the entire length of computation, see Fig. 12b (cf. Fig. 9b).

Another case where the error profiles appear flat is that of the mixed boundary conditions. For example, Fig. 12c corresponds to a problem where five faces of the cube still have Neumann boundary conditions whereas on the sixth face we set a Dirichlet boundary condition. Even though this setting differs from the pure Neumann problem by the type of the boundary condition only on one face of the cube, it already eliminates the error growth. We have also carried out additional "weaker" simulations, increasing the number of faces with Dirichlet boundary conditions all the way up to the full Dirichlet problem, with no sign of error accumulation.

We thus conclude that the growth of the error observed in Fig. 12a (see also Fig. 9a) can unambiguously be attributed to the full Neumann boundary conditions. A qualitative explanation of this error growth may be given as follows. The function $a+bt$, where a and b are constants, satisfies both the homogeneous wave equation and homogeneous Neumann boundary conditions. The constants a and b can be interpreted as the solution and its first time derivative averaged over the spatial domain Ω at $t=0$. Therefore, if the initial data (at $t=0$) for a given Neumann problem have a non-vanishing mean a and/or non-vanishing mean time derivative b, then the solution for $t>0$ may have a component $a+bt$ that grows over time unless $b=0$. As a simple physical illustration of such a solution in the one-dimensional case, one can think of the oscillations of a string with free endpoints, where the Neumann conditions correspond to a force applied to those endpoints. Then, the constant a represents the initial location of the string's center of mass and b yields the string's initial momentum. If $b\neq 0$, the overall motion of the string can be decomposed into the motion of its center of mass according to the law of classical mechanics: $a+bt$, and the oscillations in the center-of-mass moving frame. In our simulations, even though the initial mean time derivative of the reference solution (54) vanishes at $t=0$ (due to a symmetry with respect to the origin), the round-off errors may still lead to an effective non-zero b and hence to the observed linear growth of the error.

Note that in the case of Dirichlet, Neumann, or Robin boundary conditions (2c), the solution of IBVP (2) can be written in the form of a Fourier series, see [44, Chapter 2]. In particular, if (2c) is a homogeneous Neumann boundary condition ($\phi=0$), then the series takes the form:

$$u(\boldsymbol{x},t)=a_0+b_0t+\sum_{s=1}^{\infty}(a_s\cos\lambda_s t+b_s\sin\lambda_s t)v_s(\boldsymbol{x}), \tag{A.1}$$

where $v_s(\boldsymbol{x})$ are Neumann eigenfunctions of the Laplacian on Ω and $-\lambda_s^2$ are the corresponding eigenvalues. Under certain constraints on regularity and compatibility of the initial data u_0 and u_1 in (2b), series (A.1) can be proven to converge uniformly with respect to $\boldsymbol{x}$ and t, along with the series obtained by its term-wise differentiation. Then, the sum of series (A.1) yields a classical solution of IBVP (2).

The linear growth of the error that we observed in our Neumann simulations shall therefore be attributed to the first two terms of the series (A.1): a_0+b_0t. They correspond to $\lambda_0=0$ and $v_0(\boldsymbol{x})=\text{const}$. In contradistinction to (A.1), for the boundary conditions other than Neumann the solution is given by a series that contains neither a constant nor linear term:

$$u(\boldsymbol{x},t)=\sum_{s=1}^{\infty}(a_s\cos\lambda_s t+b_s\sin\lambda_s t)v_s(\boldsymbol{x}). \tag{A.2}$$

In formula (A.2), $v_s(\boldsymbol{x})$ are eigenfunctions of the Laplacian subject to the appropriate boundary condition (Dirichlet or Robin). Series (A.2) convergence uniformly under the same conditions as guarantee the convergence of series (A.1), see [44, Chapter2]. Unlike (A.1), formula (A.2) does not allow error growth over time.

References

[1] R.E. Kleinman, G.F. Roach, Boundary integral equations for the three-dimensional Helmholtz equation, SIAM Rev. 16 (1974) 214–236.
[2] A.P. Calderon, Boundary-value problems for elliptic equations, in: Proceedings of the Soviet–American Conference on Partial Differential Equations in Novosibirsk, Fizmatgiz, Moscow, 1963, pp. 303–304.
[3] R.T. Seeley, Singular integrals and boundary value problems, Am. J. Math. 88 (1966) 781–809.
[4] V.S. Ryaben'kii, Method of Difference Potentials and Its Applications, Springer Series in Computational Mathematics, vol. 30, Springer-Verlag, Berlin, 2002.
[5] George Biros, Lexing Ying, Denis Zorin, A fast solver for the Stokes equations with distributed forces in complex geometries, J. Comput. Phys. 193 (1) (2004) 317–348.
[6] Shidong Jiang, Shravan Veerapaneni, Leslie Greengard, Integral equation methods for unsteady Stokes flow in two dimensions, SIAM J. Sci. Comput. 34 (4) (2012) A2197–A2219.
[7] Mark D. Preston, Peter G. Chamberlain, Simon N. Chandler-Wilde, An integral equation method for a boundary value problem arising in unsteady water wave problems, J. Integral Equ. Appl. 20 (1) (2008) 121–152.
[8] Ha-Duong Tuong, On retarded potential boundary integral equations and their discretisation, in: Topics in Computational Wave Propagation, in: Lect. Notes Comput. Sci. Eng., vol. 31, Springer, Berlin, 2003, pp. 301–336.
[9] Víctor Domínguez, Francisco-Javier Sayas, Some properties of layer potentials and boundary integral operators for the wave equation, J. Integral Equ. Appl. 25 (2) (2013) 253–294.
[10] Daniel S. Weile, Greeshma Pisharody, Nan-Wei Chen, Balasubramaniam Shanker, Eric Michielssen, A novel scheme for the solution of the time-domain integral equations of electromagnetics, IEEE Trans. Antennas Propag. 52 (1) (Jan 2004) 283–295.
[11] Gregory Kobidze, Jun Gao, Balasubramaniam Shanker, Eric Michielssen, A fast time domain integral equation based scheme for analyzing scattering from dispersive objects, IEEE Trans. Antennas Propag. 53 (3) (March 2005) 1215–1226.
[12] Toufic Abboud, Patrick Joly, Jerónimo Rodríguez, Isabelle Terrasse, Coupling discontinuous Galerkin methods and retarded potentials for transient wave propagation on unbounded domains, J. Comput. Phys. 230 (15) (2011) 5877–5907.
[13] Francisco-Javier Sayas, Retarded Potentials and Time Domain Boundary Integral Equations. A Road Map, Springer Series in Computational Mathematics, vol. 50, Springer, Cham, Switzerland, 2016.
[14] Charles L. Epstein, Leslie Greengard, Thomas Hagstrom, On the stability of time-domain integral equations for acoustic wave propagation, Discrete Contin. Dyn. Syst. 36 (8) (2016) 4367–4382.
[15] C. Lubich, Convolution quadrature and discretized operational calculus. I, Numer. Math. 52 (2) (1988) 129–145.
[16] C. Lubich, Convolution quadrature and discretized operational calculus. II, Numer. Math. 52 (4) (1988) 413–425.

[17] Ch. Lubich, On the multistep time discretization of linear initial-boundary value problems and their boundary integral equations, Numer. Math. 67 (3) (1994) 365–389.
[18] I. Petrowsky, On the diffusion of waves and the lacunas for hyperbolic equations, Mat. Sb. (Recueil Mathématique) 17(59) (3) (1945) 289–370.
[19] M.F. Atiyah, R. Bott, L. Gàrding, Lacunas for hyperbolic differential operators with constant coefficients. I, Acta Math. 124 (1970) 109–189.
[20] M.F. Atiyah, R. Bott, L. Gàrding, Lacunas for hyperbolic differential operators with constant coefficients. II, Acta Math. 131 (1973) 145–206.
[21] S.V. Petropavlovsky, S.V. Tsynkov, Quasi-lacunae of Maxwell's equations, SIAM J. Appl. Math. 71 (4) (2011) 1109–1122.
[22] Myron Mathisson, Le probléme de M. Hadamard relatif á la diffusion des ondes, Acta Math. 71 (1939) 249–282 (in French).
[23] Christian Lubich, Achim Schädle, Fast convolution for nonreflecting boundary conditions, SIAM J. Sci. Comput. 24 (1) (2002) 161–182 (electronic).
[24] Silvia Falletta, Giovanni Monegato, An exact non-reflecting boundary condition for 2D time-dependent wave equation problems, Wave Motion 51 (1) (2014) 168–192.
[25] Silvia Falletta, Giovanni Monegato, Exact non-reflecting boundary condition for 3D time-dependent multiple scattering–multiple source problems, Wave Motion 58 (2015) 281–302.
[26] V.S. Ryaben'kii, Exact transfer of difference boundary conditions, Funct. Anal. Appl. 24 (3) (1990) 251–253.
[27] V.S. Ryaben'kii, S.V. Tsynkov, V.I. Turchaninov, Global discrete artificial boundary conditions for time-dependent wave propagation, J. Comput. Phys. 174 (2) (2001) 712–758.
[28] S.V. Tsynkov, Artificial boundary conditions for the numerical simulation of unsteady acoustic waves, J. Comput. Phys. 189 (2) (August 2003) 626–650.
[29] S.V. Tsynkov, On the application of lacunae-based methods to Maxwell's equations, J. Comput. Phys. 199 (1) (September 2004) 126–149.
[30] S.V. Petropavlovsky, S.V. Tsynkov, A non-deteriorating algorithm for computational electromagnetism based on quasi-lacunae of Maxwell's equations, J. Comput. Phys. 231 (2) (2012) 558–585.
[31] S. Petropavlovsky, S. Tsynkov, Non-deteriorating time domain numerical algorithms for Maxwell's electrodynamics, J. Comput. Phys. 336 (May 2017) 1–35.
[32] Yekaterina Epshteyn, Algorithms composition approach based on difference potentials method for parabolic problems, Commun. Math. Sci. 12 (4) (2014) 723–755.
[33] Jason Albright, Yekaterina Epshteyn, Kyle R. Steffen, High-order accurate difference potentials methods for parabolic problems, Appl. Numer. Math. 93 (2015) 87–106.
[34] S. Britt, S. Tsynkov, E. Turkel, Numerical solution of the wave equation with variable wave speed on nonconforming domains by high-order difference potentials, J. Comput. Phys. 354 (February 2018) 26–42.
[35] Steven Britt, Semyon Tsynkov, Eli Turkel, A high order compact time/space finite difference scheme for the wave equation with variable speed of sound, J. Sci. Comput. (January 2018) 1–35.
[36] M. Medvinsky, S. Tsynkov, E. Turkel, The method of difference potentials for the Helmholtz equation using compact high order schemes, J. Sci. Comput. 53 (1) (2012) 150–193.
[37] M. Medvinsky, S. Tsynkov, E. Turkel, High order numerical simulation of the transmission and scattering of waves using the method of difference potentials, J. Comput. Phys. 243 (2013) 305–322.
[38] Heinz-Otto Kreiss, Jens Lorenz, Initial-Boundary Value Problems and the Navier–Stokes Equations, Pure Appl. Math., vol. 136, Academic Press Inc., Boston, MA, 1989.
[39] Bertil Gustafsson, Heinz-Otto Kreiss, Joseph Oliger, Time Dependent Problems and Difference Methods, Pure and Applied Mathematics (New York), John Wiley & Sons Inc., New York, 1995, A Wiley-Interscience Publication.
[40] Philip M. Morse, Herman Feshbach, Methods of Theoretical Physics. 2 Volumes, International Series in Pure and Applied Physics, McGraw-Hill Book Co., Inc., New York, 1953.
[41] Henry A. Warchall, Wave propagation at computational domain boundaries, Commun. Partial Differ. Equ. 16 (1) (1991) 31–41.
[42] A.A. Reznik, Approximation of surface potentials of elliptic operators by difference potentials, Dokl. Akad. Nauk SSSR 263 (6) (1982) 1318–1321.
[43] Lloyd N. Trefethen, David Bau, III. Numerical Linear Algebra, Society for Industrial and Applied Mathematics (SIAM), Philadelphia, PA, 1997.
[44] O.A. Ladyzhenskaya, Smeshannaya Zadacha Dlya Giperbolicheskogo Uravneniya [The Mixed Problem for a Hyperbolic Equation], Gosudaerstvennoe Izdatelstvo Techniko-Teoreticheskoj Literatury, Moscow, 1953, (in Russian).
[45] Claudio Canuto, Alfio Quarteroni, Variational methods in the theoretical analysis of spectral approximations, in: Spectral Methods for Partial Differential Equations, Hampton, VA, 1982, SIAM, Philadelphia, PA, 1984, pp. 55–78.
[46] Marcus J. Grote, Imbo Sim, Efficient PML for the wave equation, arXiv:1001.0319, January 2010.
[47] Mikhail Osintcev, Semyon Tsynkov, Computational complexity of artificial boundary conditions for Maxwell's equations in the FDTD method, in: Mathematical and Numerical Aspects of Wave Propagation WAVES 2017, The 13th International Conference, Minneapolis, MN, USA, May 15–19, 2017, 2017, pp. 275–276, Book of Abstracts.
[48] H. Qasimov, S. Tsynkov, Lacunae based stabilization of PMLs, J. Comput. Phys. 227 (2008) 7322–7345.
[49] A. Fedoseyev, E.J. Kansa, S. Tsynkov, S. Petropavlovskiy, M. Osintcev, U. Shumlak, W.D. Henshaw, A universal framework for non-deteriorating time-domain numerical algorithms in Maxwell's electrodynamics, in: Michail D. Todorov (Ed.), Application of Mathematics in Technical and Natural Sciences: 8th International Conference for Promoting the Application of Mathematics in Technical and Natural Sciences — AMiTaNS'16, in: AIP Conference Proceedings, vol. 1773, American Institute of Physics (AIP), 2016, 020001, 21 pp.